# Novel Composite Materials for SOFC Cathode-Interconnect Contact

***A Final Scientific/Technical Report***

***for***

***DOE Award No. DE-FG26-05NT42533***

***Aug. 1, 2005 – July 31, 2009***

*Submitted by*

**J. H. Zhu, Principal Investigator**

Department of Mechanical Engineering
115 W. 10th Street, TTU Box 5014
Tennessee Technological University, Cookeville, TN 38505

**Report Issued in September, 2009**

## ABSTRACT

This report summarized the research efforts and major conclusions of our University Coal Research Project, which focused on developing a new class of electrically-conductive, Cr-blocking, damage-tolerant Ag-perovksite composite materials for the cathode-interconnect contact of intermediate-temperature solid oxide fuel cell (SOFC) stacks. The Ag evaporation rate increased linearly with air flow rate initially and became constant for the air flow rate ≥ ~1.0 $cm \cdot s^{-1}$. An activation energy of 280 $KJ.mol^{-1}$ was obtained for Ag evaporation in both air and $Ar+5\%H_2+3\%H_2O$. The exposure environment had no measurable influence on the Ag evaporation rate as well as its dependence on the gas flow rate, while different surface morphological features were developed after thermal exposure in the oxidizing and reducing environments. Pure Ag is too volatile at the SOFC operating temperature and its evaporation rate needs to be reduced to facilitate its application as the cathode-interconnect contact. Based on extensive evaporation testing, it was found that none of the alloying additions reduced the evaporation rate of Ag over the long-term exposure, except the noble metals Au, Pt, and Pd; however, these noble elements are too expensive to justify their practical use in contact materials. Furthermore, the addition of $La_{0.8}Sr_{0.2}MnO_3$ (LSM) into Ag to form a composite material also did not significantly modify the Ag evaporation rate. The Ag-perovskite composites with the perovskite being either $(La_{0.6}Sr_{0.4})(Co_{0.8}Fe_{0.2})O_3$ (LSCF) or LSM were systematically evaluated as the contact material between the ferritic interconnect alloy Crofer 22 APU and the LSM cathode. The area specific resistances (ASRs) of the test specimens were shown to be highly dependent on the volume percentage and the type of the perovskite present in the composite contact material as well as the amount of thermal cycling that the specimens were subjected to during testing. The Ag-LSCF composite contact materials proved more effective in trapping Cr within the contact material and preventing Cr migration into the cathode than the Ag-LSM composites. Ag-perovskite composite contact materials are promising candidates for use in intermediate-temperature SOFC stacks with ferritic stainless steel interconnects due to their ability to maintain acceptably low ASRs while reducing Cr migration into the cathode material.

## TABLE OF CONTENTS

## 1. EXECUTIVE SUMMARY

This final scientific/technical report summarized the research efforts and major conclusions for the University Coal Project "Novel Composite Materials for SOFC Cathode-Interconnect Contact", for the period of Aug. 1, 2005 – July 31, 2009. This project aimed at developing a new class of electrically-conductive, Cr-blocking, damage-tolerant Ag-perovksite composite materials for the cathode-interconnect contact of intermediate-temperature solid oxide fuel cell (SOFC) stacks.

To reduce the electrode/interconnect interfacial resistance in SOFC stacks, electrical contact layers are often applied between the interconnect and electrodes during construction of an SOFC stack by compensating for the corrugations present on their respective surfaces. Three major criteria for SOFC contact materials are: (1) sufficient high electrical conductivity over the SOFC lifetime; (2) chemical stability under high current condition and compatibility with other cell components, especially negligible effects on the formation of protective oxides on interconnect alloy; (3) reasonable match in coefficient of thermal expansion (CTE) with other cell components. Because of the stringent criteria, finding a suitable material for the interconnect-cathode contact is very challenging, particularly in the intermediate temperature (600-800°C) SOFCs where high-temperature oxidation-resistant alloys are used as interconnect material.

The materials currently under consideration for cathode/interconnect contact application includes low melting-point ceramics (such as doped $LaCoO_3$), noble metals (e.g. Ag or Pt), and their composites. Pt, Au, and Pd are not desirable for this application because of their high raw material cost. However, Ag is an exception due to its relatively low price. Ag-ceramic composite is one of the very promising candidates for SOFC contact due to the inherent properties of Ag, such as high chemical stability, high electrical conductivity, high ductility, and relatively low melting point. The perovskite component in the composite is expected to provide more desirable CTE match and act as a Cr absorbent and/or a barrier for Cr migration to the cathode. One major drawback of Ag as SOFC interconnect/cathode contact material is its tendency to evaporate at the SOFC operating temperatures and subsequent migration to other cell components, potentially causing the cell performance degradation.

To date, the evaporation behaviors of Ag under SOFC operating conditions has not been systematically investigated, even though numerous studies have been carried out on thermal etching of Ag at elevated temperatures. In this study, the effects of exposure time/temperature, gas flow rate, and environment on the evaporation of pure Ag at 750-900°C were studied systematically. The Ag evaporation rate increased linearly with air flow rate initially and became constant for the air flow rate $\geq \sim 1.0$ $cm \cdot s^{-1}$. An activation energy of 280 $KJ.mol^{-1}$ was obtained for Ag evaporation in both air and $Ar+5\%H_2+3\%H_2O$. The exposure environment had no measurable influence on the Ag evaporation rate as well as its dependence on the gas flow rate, while different surface morphological features were developed after thermal exposure in the oxidizing and

reducing environments. Clearly, pure Ag is too volatile at the SOFC operating temperature and its evaporation rate needs to be reduced via certain approaches.

Two potential approaches for mitigating the Ag evaporation were assessed with regard to their viability: (1) alloying addition to form Ag-base alloys and (2) addition of perovskite to form Ag-perovskite composites. A number of Ag-base alloys were prepared and their evaporation behaviors were evaluated. Based on extensive evaporation testing, it was found that none of the alloying additions including Ti, Co, Fe, Ni, Mn, Sn, Si, Al, Sb, Y, Zr, etc., reduced the evaporation rate of Ag over the long-term exposure. The only alloying additions that effectively decreased the Ag evaporation rate were the noble metals Au, Pt, and Pd. However, these elements are too expensive to justify their practical use in contact materials. Furthermore, the addition of $La_{0.8}Sr_{0.2}MnO_3$ (LSM) into Ag to form a composite material also did not significantly modify the Ag evaporation rate. This can be attributed to the fact that these composites were quite porous and Ag could escape from the composite materials via the interconnected voids.

Since composite materials can have a dramatic effect on SOFC performance by combining the unique attributes from each constituent material, a major opportunity exists for significant improvement in SOFC performance with a noble metal/ceramic composite contact material, provided a material can be developed which combines the Cr-absorbing/blocking characteristics of the perovskite phases, with the excellent electrical and mechanical properties of a noble metal, while maintaining the overall relatively low cost of the contact material. In this study, the Ag-perovskite composites with the perovskite being either $(La_{0.6}Sr_{0.4})(Co_{0.8}Fe_{0.2})O_3$ (LSCF) or LSM were also systematically evaluated as the contact material between the ferritic interconnect alloy Crofer 22 APU and the LSM cathode. The area specific resistances (ASRs) of the test specimens were shown to be highly dependent on the volume percentage and the type of the perovskite present in the composite contact material as well as the amount of thermal cycling that the specimens were subjected to during testing. The chromium content present in both the contact layer and the adjacent cathode material was measured after testing, and the Ag-LSCF composite contact materials proved more effective in trapping Cr within the contact material and preventing Cr migration into the cathode than the Ag-LSM composites. Ag-perovskite composite contact materials are promising candidates for use in intermediate-temperature SOFC stacks with ferritic stainless steel interconnects due to their ability to maintain acceptably low ASRs while reducing Cr migration into the cathode material.

## 2. REPORT DETAILS

### 2.1 Experimental Methods

#### *2.1.1 Alloy Preparation and Evaporation Testing*

The evaporation experiments of pure Ag were performed using polycrystalline Ag coupons a purity of 99.95 wt.%. The Ag-base alloys were prepared in our laboratory using the silver shot from Alfa Aesar and other elements from either Alfa Aesar or Atlantic Equipment. The correct amount of each element was weighed and placed in an arc-melter. The melting chamber was allowed to reach a rough vacuum and flushed with argon four times. The pressure in the chamber was allowed to rise to 5 inHg and the melting procedure began. Each alloy was melted six times, flipping the sample between each melt, to ensure consistent melting and thorough mixing. The samples were allowed to cool in the water cooled crucible for 15 minutes and subsequently removed and re-weighed to check for losses during melting. A total of 25 different alloys were produced by the above method. 3, 5, 10 and 15 at.% alloying elements were mixed, pressed, and sectioned into ~ 1 x 1 x 0.1 cm coupons. In addition, several Ag-LSM composites with different Ag:LSM ratios were also prepared for evaluation. Before testing, the samples were ground on all sides to 1200 grit finish and a 1 mm hole drilled in the upper center of the samples.

The sample dimensions were measured and then ultrasonically cleaned, both in water and in acetone for 5 minutes each. Each sample was then weighed with a high accuracy balance to ±0.00005 g. They were then hung in a quartz fixture and placed in a horizontal furnace as shown in the schematic drawing, Figure 1. Moist air with a velocity of 1.3 $cm \cdot s^{-1}$ was flown at all times across the samples and they were heated at 5 $°C \cdot min^{-1}$ until 800, 850 or 900°C was reached, depending on the sample set. This temperature was initially held for 40 hours. Some coupons were tested for longer duration. After reaching a temperature below 200°C, so as not to shock the fixture, the samples were removed and weighed. For the pure Ag, the evaporation experiments were conducted in air, air+3%$H_2O$ (humidified air – a simulated cathode environment), as well as in the reducing environment of Ar+5%$H_2$ or Ar+5%$H_2$+3%$H_2O$ (a simulated anode environment) and the flow rate was varied in the range of 0 - 2.5 $cm \cdot s^{-1}$ using a gas flowmeter. The surface morphology and cross-sectional views of some coupons were observed in a scanning electron microscope (SEM) equipped with an energy-dispersive spectroscope (EDS).

#### *2.1.2 Preparation of Ag-Perovskite Composites and Test Cells*

Figure 2 shows a schematic drawing of the test cell. Basically, dense LSM pellets were used as supports. The LSM powder, obtained from NexTech Materials, was pressed at 150 MPa in a 19-mm diameter die. The green bodies, weighing about 1.6 grams, were heated to 900°C at 3°C/min and held for one hour before further heating to 1400°C at 5°C/min. These sintered pellets of around 16-mm in diameter and 1.2-mm thick were

polished on both sides to an 800-grit finish. The cathode layer was prepared by screen-printing with an LSM ink and sintering at 1100°C for one hour, which produced a porous cathode with a thickness of around 20 μm.

The composite contact materials investigated in this study included several Ag-perovskite composites with various volume percentages (vol.%) of perovskite, which was either $La_{0.6}Sr_{0.4}Co_{0.8}Fe_{0.2}O_3$ (LSCF) or LSM. For the Ag-LSCF composites, the content of LSCF was 0, 25, 50, 75, or 100 vol.%. For the Ag-LSM composites, the content of LSM was 25, 50, 75, 90, or 100 vol.%. The composites were fabricated by hand mixing the powders in the desired proportions using a mortar and pestle, followed by ball-milling the mixture overnight. The mixed powders were brushed through a 200-mesh sieve to ensure a small particle size before being mixed with an ink vehicle to form a paste suitable for screen-printing. Crofer 22 APU coupons, measuring 13-mm in diameter and 0.6-mm thick, were polished to an 800-grit finish on both sides. The composite contact layer of approximately 60-μm thick was placed between the LSM cathode and the Crofer 22 APU interconnect via screen-printing, as shown in Fig. 2.

### *2.1.3 ASR and Microstructural Characterization*

The contact materials were evaluated with regard to the ASR change during thermal exposure. A test fixture was constructed to facilitate the simultaneous testing of six specimens. The fixture utilized six alumina tubes with spring-loaded internal alumina rods mounted to an aluminum base. A compressive load of 0.16 kg/cm$^2$ was applied to simulate a stack environment. A schematic showing the internal design of an individual cell holder can be seen in Fig. 3. A thermocouple was placed at the center of the fixture, level with the test cells for accurate control of the test temperature.

Test cells were wired according to the four-probe method with platinum leads as shown in Fig. 2. Two upper leads were spot-welded to the Crofer 22 APU and two lower leads were attached to the Pt patch for current collection. Six Agilent DC power supplies were used to apply a constant current density of 250 mA/cm$^2$ across the cells via one upper and one lower lead, while a LabVIEW program was used in conjunction with a multi-channel Keithley 2700 multimeter to measure and record the voltage drop across each cell every five minutes during testing via the remaining two leads. For stationary SOFC stack applications, isothermal holding with occasional thermal cycling will be the typical operating state, while for mobile applications, repeated thermal cycling with relatively short holding times will be encountered. For this reason, two types of testing, isothermal exposure and thermal cycling, were carried out to mimic the typical thermal conditions for stationary and mobile SOFC stack operations, respectively, and to estimate the cell ASR response in such realistic application conditions. At the beginning of each test, the cell was heated to 850°C and held for 10 h to facilitate the initial sintering of the contact paste. The cell temperature was then dropped to 800°C, followed by either thermal cycling or isothermal exposure. For cyclic exposure, each cycle consisted of holding at 800°C for 10 h before furnace cooling to 250°C and subsequent heat-up to 800°C. A total of 50 thermal cycles (or 500 cumulative hours of exposure at 800°C) were

completed for each group of test cells. For isothermal exposure, the cells were held at 800°C for 250 h, furnace cooled to 250°C and then heated and held at 800°C for another 250 h. Several additional cells were tested under the same isothermal exposure conditions for the same duration without current applied to them to assess the effect of current on the oxidation of the interconnect alloy as well as the Ag migration behavior of the contact layers.

After thermal exposure was completed, the test cells were mounted, cross-sectioned, and examined with SEM/EDS. The oxide scales formed on the interconnect alloy after thermal exposure were observed carefully for all the cells. Abnormal scale growth was noticed for some cells. In addition, the phase evolution and morphological features of the microstructure in the contact layer and the cathode were assessed, particularly with regard to Ag migration. Another aspect of interest is the detection of Cr migration throughout the cell during the thermal exposure. EDS analyses of the average chemical composition of the contact layer as well as the porous cathode area were conducted to quantify the Cr content in each layer. This allowed for rough estimate and comparison of the Cr-blocking and absorbing capabilities of each contact material.

## 2.2 Results and Discussion

### *2.2.1 Evaporation Behaviors of Pure Ag*

To investigate the effect of exposure time on Ag evaporation, the Ag samples were heated at 900°C either in stagnant air, flowing air or flowing Ar+3%$H_2$+3%$H_2O$ with a flow rate of 1.56 cm.$s^{-1}$ for different durations. As shown in Fig. 4, the weight losses of Ag at 900°C in stagnant air as well as in a flowing air with a flow rate of 1.56 cm.$s^{-1}$ exhibited good linear relations with the duration of thermal exposure, indicating that a constant evaporation rate was obtained for each of the two cases. Also, the air flow increased the Ag evaporation rate significantly. Furthermore, as shown on Fig.4, an identical constant evaporation rate was observed in the reducing environment as in the flowing air at the same gas flow rate. The existence of a constant evaporation rate under a fixed exposure condition, consistent with prior experimental results [1], makes it possible for direct comparison of evaporation results obtained with different exposure durations. The linear relationship between the weight loss and the duration of thermal exposure also implies that the weight loss during heating and cooling is negligible compared to the weight loss during isothermal holding.

To the best of our knowledge, no work has been performed so far to take the gas flow rate into consideration in the study of Ag evaporation. It is postulated that many controversies in the literature related to Ag evaporation might be due to the difference in gas flow rate or residual gas pressure in a vacuum. As shown in Fig. 5, the evaporation rate of pure Ag, calculated from the weight loss data after a 50-hour exposure in air at both 900 and 850°C, initially increased linearly with air flow rate and then reached a plateau at a flow rate of about 1.0 cm·$s^{-1}$. Further increase in air flow rate had no effect on the Ag evaporation, i.e. a constant evaporation rate was observed. The evaporation rate at the flow rate above 1.0 cm.$s^{-1}$ was about 2.6 times that in stagnant air for exposure at both 850 and 900°C. Hondros and Moore [2] found that Ag crystals heated in vacuum

exhibited a loss of weight about 100 times greater than that after heating in open air at the same temperature. It was also found that the evaporation rate was approximately doubled in nitrogen compared to that in air; however, the flow rate of nitrogen and air was not mentioned in their paper. The enhanced evaporation at a high air flow rate or in vacuum was most likely due to the less re-condensation of the Ag vapor over the sample, since a high flow rate carried the Ag vapors away from the sample more efficiently, resulting in accelerated evaporation.

When the flow rate reached the critical value (1.0 $cm.s^{-1}$), the evaporation of Ag is essentially controlled by the evaporation process alone. As a result, the evaporation rate remained constant. When the evaporation temperature increased from 850 to 900°C, the evaporation rate corresponding to the plateau increased significantly due to the increased Ag vapor pressure, while the critical flow rate was the same. Similar effects of air flow rate were observed on the Cr evaporation from $Cr_2O_3$ [3]. Also shown in Fig. 5 are several data points for the Ag evaporation rate in Ar+3%$H_2$+3%$H_2O$ at 900°C. These data points clearly overlap with those obtained in air, i.e. an essentially same effect of the flow rate on the Ag evaporation rate was obtained in the reducing environment as in air, which confirms that the evaporation environment had negligible influence on the Ag evaporation behavior.

A relatively high air flow rate of 1.56 $cm.s^{-1}$ was selected as a standard flow rate for evaluating the effect of temperature on Ag evaporation rate and the test temperature was varied from 750 to 925ºC. It was found that the Ag evaporation rate increased significantly with exposure temperature. A linear relationship was obtained between the Ag evaporation rate in log scale and the reciprocal of temperature, as shown in Fig. 6. The activation energy for Ag evaporation, calculated from the slope of the straight line, was equal to 280 $kJ.mol^{-1}$. Furthermore, the same activation energy was obtained in Ar+5%$H_2$+3%$H_2O$ using the data in Fig. 6, i.e. the activation energy for Ag evaporation did not change with the testing gas environments. These results were in good agreement with the data from the effusion measurements by McCabe and Birchenall [4]. Winterbottom [5] also studied the evaporation of single crystal of Ag in a vacuum of $10^{-8}$ torr and found that the heats of vaporization for (111) and (100) orientations were 279.2 and 278 $KJ.mol^{-1}$, respectively. The essentially identical activation energy implies that the same vaporation mechanism is operating under these conditions and the evaporation of Ag is controlled by breaking the bonding between the Ag atoms on the solid surface.

Several evaporation experiments were carried out in the presence of various vapor phase constituents, i.e. air, air+3%$H_2O$, Ar+5%$H_2$, or Ar+5%$H_2$+3%$H_2O$ with a same flow rate of about 1.56 $cm.s^{-1}$. The results, as given in Table 1, once again indicate that the exposure atmosphere had a negligible influence on the evaporation of Ag, which is in agreement with that of Winterbottom [5], who found that the flux of silver atoms in a high-vacuum environment was strictly a function of the surface temperature and it was not perturbed by an ambient gas, a return flux of silver, or the sample surface orientation. However, Leroux and Raub [6] observed no weight loss when Ag was exposed at high temperatures to reducing or inert atmospheres. On the other hand, Meulenberg et al. [7] recently reported significantly different evaporation rates in humidified air and in the reducing environment of Ar+4%$H_2$+3%$H_2O$, with the reducing environment causing

almost one order of magnitude reduction in Ag evaporation rate. In their evaporation tests, Ag meshes with a wire diameter of 0.35 mm were used, in contrast to the bulk Ag plates used in this study. More work is needed to rationalize these different observations.

**Table 1 Evaporation rates of Ag in various atmospheres at 900°C with a gas flowing rate of 1.56 cm.s$^{-1}$**

| Atmosphere | Evaporation Rate ($10^{-9}$ g.cm$^{-2}$.s$^{-1}$) |
|---|---|
| Ar+5%$H_2$+3%$H_2O$ | 7.12 |
| Ar+5%$H_2$ | 7.06 |
| Air+3%$H_2O$ | 7.22 |
| Air | 7.11 |

Since the Ag samples were cooled prior to examination, it is essential to consider the extent to which the morphological features recorded actually represent the true surface morphology at the evaporation temperature. Evaporation as well as surface and volume diffusion will occur during cooling, and the extent to which these transport process can alter the surface will limit the features that can be used to characterize the surface morphologies upon thermal evaporation. Fortunately, this concern was resolved both theoretically and experimentally by Winterbottom [5] and Chalmers [8], who proved that the surface and volume transports during cooling have a negligible influence on the morphological features developed during isothermal holding. Our present evaporation results at various temperatures also indicate that, for each temperature drop of 100°C, the evaporation rate of Ag decreased orders of magnitude. As shown in Fig. 7, all sample surfaces developed a faceting or striation structure (parallel ledges) after thermal exposure in air at temperatures from 750 to 900°C. The spacing between the ledges increased with the exposure temperature. However, Ag samples exhibited very smooth, featureless surface, with only some thermal grooving observed near the grain boundaries, after thermal exposure in both Ar+5%$H_2$ and Ar+5%$H_2$+3%$H_2O$, see Fig. 8 as an example.

There are two major hypotheses for the formation of striations on the Ag surface after thermal evaporation in oxygen-containing atmospheres. One hypothesis is that Ag evaporation is enhanced at certain low-index orientations, such as {111}, {100}, or {110}. During thermal evaporation, these low-index orientations will evaporate faster than the other high-index orientations, therefore achieving a hill-and-valley structure. The typical evidence was presented by Hondros and Moore [2], who found that when the net weight loss was prevented, the surface of Ag was not etched, i.e. a smooth surface with grain boundary grooves existed after thermal exposure. The second hypothesis is the so-called minimum surface energy theory. According to the Wulff construction theory [9], the equilibrium shape is determined by

$$\frac{\gamma_1}{h_1} = \frac{\gamma_2}{h_2} = \cdots = \frac{\gamma_i}{h_i} \qquad (1)$$

where $h_i$ and $\gamma_i$ are the distance and surface energy of plane *i* from the center of the crystal. It has been shown that $\frac{\gamma_{\{100\}}}{\gamma_c} = 0.90$ and $\frac{\gamma_{\{111\}}}{\gamma_c} = 0.84$, where $\gamma_c$ is the surface energy for a random plane [10]. During thermal evaporation, these low surface energy planes will be formed to minimize the total surface energy.

According to our results, the exactly same weight loss was registered in air and the reducing environment when other exposure conditions were kept identical. However, the striation structure was only formed in air, while for the samples exposed to the reducing environment a smooth surface was observed, implying that the difference in evaporation rate is not the true cause for striation formation. Therefore, it is most likely that the formation of striation structure is due to the formation of planes with minimal surface energy. Why oxygen must be present to form the surface planes with minimal energy is still unclear. A possible explanation is that when $O_2$ is present, it might be preferentially absorbed on the low-index planes such as (111) or (100) and the oxygen absorption on these planes can significantly lower the surface energies of these planes, resulting in striation formation.

Ag is a very promising material for SOFC contact application because of its many inherent properties, such as high electrical and thermal conductivity, excellent ductility, and high chemical stability, good sinterability, etc. However, the evaporation of Ag and its subsequent migration to the other cell components might prevent this material from being used for this application. For example, our results indicate that at an air flow rate of 1.1 $cm.s^{-1}$ and a temperature of 800°C (i.e. the typical SOFC cathode condition), the evaporation rate of Ag is ~$4.4x10^{-10}$ $g.cm^{-2}.s$. A simple calculation shows that after thermal exposure at 800°C over the targeted SOFC lifetime of 40,000 h, the loss of Ag will be about 0.063 $g.cm^{-2}$ or 63 μm in thickness. Considering the porous nature of the contact material as well as a nominal thickness of 40-100μm for the contact layer, most of the Ag in the contact layer will be evaporated and disappeared after the service. Thus, pure Ag is not suitable for the cathode/interconnect contact application, because of its excessive evaporation in the SOFC operation conditions.

### *2.2.2 Evaporation Behaviors of Ag-Base Alloys and Ag-Perovskite Composites*

The results of the evaporation rates of various Ag-base alloys during the first 40 hours are tabulated in Tables 2-3. According to Table 2, the addition of 1 at.% Al, Si, and Mn led to the reduction in evaporation rate on the order of 57%, 16%, and 33%, respectively. Al and Si were oxidized to form the insulating $Al_2O_3$ and $SiO_2$; therefore, the alloys containing Al or Si were not studied further. For the Ag alloys with 3% alloy additions, the Ag-3% Mn alloy exhibited a gain in weight (i.e. the negative apparent evaporation rate denoting a gain in weight rather than the usual loss), while the Zn-contained alloy

evaporated like pure Ag. From Table 3, many alloys with 5 and 15% alloying additions exhibited a negative evaporation rate, which obviously is due to the pick-up of the oxygen form the environment and the resultant weight increase of the sample.

**Table 2 Evaporation rates of Ag-1% X and Ag-3% X alloys**

| Composition (at.%) | Evaporation rate ( x $10^{-9}$ g/(cm²*s)) |
|---|---|
| 100% Ag | 7.32 |
| Ag-1% Al | 3.13 |
| Ag-1% Zn | 7.88 |
| Ag-1% Mg | 8.4 |
| Ag-1% Mn | 4.92 |
| Ag-1% Ti | 8.1 |
| Ag-1% Si | 6.17 |
| Ag-3% Mn | -4.19 |
| Ag-3% Zn | 8.35 |

**Table 3 Evaporation rates of Ag-5% X and Ag-15% X alloys**

| Composition (at.%) | Evaporation rate ( x $10^{-9}$ g/(cm²*s)) |
|---|---|
| Ag-5% Mn | -1.97 |
| Ag-5% Zn | 4.67 |
| Ag-5% Ti | -3.75 |
| Ag-5% Co | 6.66 |
| Ag-5% Ni | 3.71 |
| Ag-5% Fe | 7.34 |
| Ag-5% Sn | -2.91 |
| Ag-15% Mn | -8.66 |
| Ag-15% Ti | -1.69 |
| Ag-15% Co | -1.65 |
| Ag-15% Ni | -6.04 |
| Ag-15% Fe | -2.05 |

Both the initial reduction in evaporation rate and the negative evaporation rate for the Ag-base alloys could be attributed to the growth of an oxide layer near the surface of the samples. These oxide layers formed with the diffusion of oxygen from the environment into the samples, consuming the alloying element and transforming it into an oxide. Examples of the cross-sectional views for the Ag-Mn alloys are shown in Figs. 9 and 10.

Unfortunately, the oxide layers formed on the sample surface were quite porous and as a result they were not effective in blocking the Ag evaporation. Indeed, long-term exposure confirmed that the Ag evaporation rates of these alloys were essentially similar to that of pure Ag, as shown in Fig. 11. The long-term tests of >150 hours were conducted on pristine samples of the same compositions that showed negative evaporation rate in their first test. While during the initial testing the alloying elements

were completely oxidized to from metal oxide which caused a weight gain, Ag continued to evaporate at the rate of pure Ag due to the porous nature of the metal oxide.

The Ag evaporation behaviors of the Ag+LSM composites with different Ag-to-LSM ratios was also evaluated at 900°C in a moist air with a flow rate of 1.3 cm/s. The most obvious conclusion is that the addition of LSM into Ag to form a composite material did not significantly modify the Ag evaporation rate. This can be attributed to the fact that these composites were quite porous and Ag could escape from the composite materials via the interconnected voids.

### *2.2.3 ASR Response of the Cells with the Composite Contacts*

Figures 12 and 13 depict the isothermal ASR behaviors of Ag-LSCF and Ag-LSM, respectively, over 500 hours with a single cool-down event after 250 h. For ease of reading, the ASR data for the cool-down periods are not included in any of the ASR figures; however, it is still clearly evident where the thermal cycles took place due to the obvious breaks in the data. The ASRs of the composites generally increased with ceramic content in the composite contact layer due to the lower electrical conductivity of the perovskite compared to Ag. A step increase in ASR for the contact materials with 50 vol.% or greater perovskite was observed after the single thermal cycle, confirming that thermal stress generation and subsequent cracking resulting from the mismatch in CTE is the primary mechanism for ASR degradation in ceramic contact materials [11]. These thermal stresses are commonly present in SOFC stacks and are probably exacerbated by the compressive loads normally applied to the stacks.

Figure 12 clearly shows the self-healing characteristics of the Ag-LSCF composites after damage was incurred from one thermal cycle. Even for contact materials with 50 vol.% or greater LSCF content, there was a substantial amount of healing that took place after the thermal cycle at 250 hours. In fact, the ASRs of all of the contact materials were still decreasing during the final 100 hours of cell testing. This self-healing ability is obviously desirable for SOFC applications where continuous operation is not feasible. The self-healing behavior exhibited in the Ag-LSCF and Ag-LSM composites could be attributed to the sintering activity of the respective ceramics, most likely assisted by Ag. It has been widely reported that LSCF is sinterable at temperatures as low as 700°C, which explains why the cells with the Ag-LSCF contact materials showed a gradually decreasing ASR once the cells were returned to their operating temperature of 800°C [12-14]. LSM, on the other hand, requires sintering temperatures in excess of 1100°C to achieve adequate densification and electrical conductivity [15-17]. This clarifies why the LSM contact materials did not exhibit self-healing behavior after the thermal cycle (Figure 13), while the Ag-LSM composites exhibited a much reduced self-healing capability compared to the Ag-LSCF composites with the same amount of Ag.

Figure 14(a) shows the ASR response of the test cells with the Ag-LSCF composite contact materials during thermal cycling. The data clearly demonstrates a trend of decreasing ASR with increasing Ag content in the contact material, similar to what was observed under isothermal conditions. Also, the rate of ASR increase (i.e. ASR

degradation rate) decreased with increasing Ag content. These trends are considered to be indicative of the ability of Ag to deform and relax thermal stresses encountered during thermal cycling. For the contact materials with 50% LSCF or greater, a degree of self-healing was seen during the isothermal hold periods. It can be seen that the 50% LSCF contact material exhibited a steadily decreasing overall ASR throughout the test, while the 75% LSCF contact material exhibited a slowly increasing overall ASR. The higher amount of Ag in the 50% LSCF contact layer mitigated the thermal stresses generated during thermal cycling more effectively than the 75% LSCF contact, which resulted in less ASR degradation between cycles to recover from and therefore a lower ASR degradation rate. The self-healing behavior is most easily visible in the 100% LSCF contact material, where each cycle can be seen as a step increase in ASR at the beginning of each cycle due to the damage introduced to the cell during cycling when the temperature was reduced to 250°C and then raised back to 800°C. The step increase was followed by a gradual reduction in ASR during the isothermal holding period. There is a certain amount of damage that occurred during each thermal cycle that could not be fully recovered during the 10-hour isothermal holding period, resulting in an overall trend of ASR increase during thermal cycling. It is possible that with longer isothermal holding periods, most or all of the damage incurred during the cool-down can be recovered

Figure 14(b) shows the ASR response of the cells with the Ag-LSM composite contacts during thermal cycling. These contact materials exhibited the same trends as the Ag-LSCF contact materials with regard to the relationship between ASR and the Ag content in the composition. Even with the 90% LSM contact material, an order-of-magnitude drop in both ASR and ASR degradation rate was observed when compared to the 100% LSM contact material. It can be also observed from Fig. 14 that the contact materials with greater than 50% LSM content exhibited a step increase in ASR between cycles, followed by a relatively stable ASR during the 10-h isothermal holding period. The self-healing with regard to ASR observed in the Ag-LSCF composites was not as noticeable for these Ag-LSM composites.

It is important to relate the cell ASR with these contact materials to the long-term performance goals desired by industries. An operating lifetime of 40,000 hours is expected for stationary SOFC stacks and an overall ASR not exceeding 100m$\Omega$/cm$^2$ is desired for interconnects [18,19]. By comparing the rate of ASR change during the last 100 hours of cell testing (i.e. 400-500 h), a stark contrast was observed between thermally-cycled and isothermally-held specimens. As can be seen in Fig. 15, the degradation rate of the isothermally-held contact materials was much lower than that of the thermally-cycled contact materials, especially for the materials with greater than 50% ceramic content. It should be noted that some of the ASR degradation rates were negative in the figure, which indicates that the overall ASR was still decreasing during the final 100 hours of testing as a result of the self-healing behavior of the contact material. In order to meet the lifetime requirement of less than 100 m$\Omega$/cm$^2$, contact materials with at least 50% Ag must be used in cells subjected to frequent thermal cycling while it is possible for cells with less than 25% Ag content to be used for applications with extended periods of isothermal holding.

### *2.2.4 Microstructural Evaluation*

Figure 16 is a micrograph showing the cross section of a typical composite contact material test cell after isothermal exposure. In this case, there are no unusual features that are readily apparent from the microstructure. During thermal exposure, Crofer 22 APU is known to form a very stable, slow-growing oxide scale with a $(Mn,Cr)_3O_4$ spinel outer layer atop a thin $Cr_2O_3$ inner layer [20]. However, for some of the cells under cyclic exposure, a very thick (~60 μm), irregular oxide scale was observed on the surface of the Crofer interconnect on the side in contact with the contact layer. This phenomenon is most noticeable on the test cells with 100% LSM contact material, as shown in Fig. 17; however, the cells with 100% LSCF contact material and many of the Ag-LSM and Ag-LSCF composites also exhibited abnormal oxide scales up to ~25 μm thick. This oxidation behavior is very atypical of Crofer 22 APU and was only seen on the cathode side; normal oxidation behavior was observed for the interconnect of the same cells on the side opposite from contact material, with a scale thickness of < 3 μm after 500 hours of cumulative thermal exposure, as shown in Fig. 18.

Thermally-induced stresses due to the extreme thermal cycling and the inability of the ceramic contact materials to deform was assumed to have caused cracking in the protective $Cr_2O_3$ layer thermally grown on the interconnect on the cathode side, allowing further oxidation to occur on the exposed interconnect surface. The 100% LSCF contact material was shown to have significant amounts of cracking within the contact layer, while the 100% LSM contact material did not. It is believed that the cracking within the contact layer mitigated the thermal stresses developed during thermal cycling and thus reduced the extent of the cracking in the protective $Cr_2O_3$ scale. If the repeated thermal cycling is the primary cause of the abnormal oxidation, then samples subjected to isothermal holding with only one thermal cycle should exhibit substantially less abnormal oxidation, which was proven to be the case, as seen in Fig. 19 where one of the worst locations was shown. Although there are still some regions with severe attacks on the Crofer 22 APU alloy, the severity of the phenomenon was greatly reduced, as only one thermal cycle was involved. Analysis of the abnormal oxide scale revealed a thin, discontinuous $(Mn,Cr)_3O_4$ spinel outer layer with an adjacent thin $Cr_2O_3$ layer. The bulk of the oxide layer was porous $Fe_2O_3$, with an additional porous, Fe-depleted $Cr_2O_3$ layer at the interconnect/oxide interface. An EDS line scan illustrating the compositional profile in this oxide scale can be seen in Fig. 20.

Even though Ag has a much higher CTE compared to the perovskite, interconnect, and the cathode, the abnormal oxidation gradually diminished as the Ag content in the composite increased. This can be explained by the fact that Ag is very ductile and could easily deform under stress, which will reduce the thermal stress level and potentially avoid the cracking of the protective $Cr_2O_3$ scale.

Another interesting observation with cross-sectional analysis was made on the Ag-containing contact materials. There appeared to be a substantial amount of Ag migration into the cathode material that occurred during cell testing. This is especially clear for the high Ag-content contact materials, as can be seen in Fig. 21. Ho and Huntington [21] as well as others [22,23] have reported that Ag is susceptible to mass transport at high temperatures under an applied electric field by a process called electromigration.

However, further analysis of the phenomenon using EDS shows that it was not a pure Ag phase, but rather Ag-Cr-Mn-O compounds that were present in the cathode. Furthermore, an identical test with the same contact materials under zero applied current indicates that no significant difference could be noticed for the contact materials under zero and 250 $mA/cm^2$ applied current density, as there was a large amount of the Ag-Cr-Mn-O phase present in the cathode material for both the test cells. Clearly, electromigration of Ag is not the key contributor to the presence of the Ag-rich phase in the cathode.

Both $AgCrO_2$ and $Ag_2CrO_4$ could be formed as a result of the interaction between Ag and Cr in oxidizing environments at elevated temperatures [24-26]. EDS analysis of our tested cells revealed the presence of both of these compounds at room temperature. The dominant phase, which was observed both in the contact layer and the porous cathode, was $Ag_2(Cr,Mn)O_4$, while only very small amounts of $Ag(Cr,Mn)O_2$ were detected in the contact layer.

Figures 21 and 22 show the presence of two phases, $Ag_2(Cr,Mn)O_4$ and $Ag(Cr,Mn)O_2$, in the 100% Ag contact material, and it is quite clear that the majority of the new phase observed is $Ag_2(Cr,Mn)O_4$. $Ag_2CrO_4$ is readily formed by reaction of Ag with Cr-containing vapors at elevated temperatures; this reaction, reported by Abernathy et al., can be seen below [26]:

$$\tfrac{1}{2}\, O_2 + CrO_2(OH)_2 + 2\, Ag \rightarrow Ag_2CrO_4 + H_2O \qquad (1)$$

The compound $Ag_2CrO_4$ is known to have a decomposition temperature of 665°C [25,26], which is well below the melting temperature of pure Ag (962°C) [27], and also well below the test temperature of our cells (800°C). After reaching its decomposition temperature, $Ag_2CrO_4$ is expected to convert to $AgCrO_2$ and Ag, following the reaction below [25].

$$Ag_2CrO_4 \rightarrow AgCrO_2 + Ag + O_2 \qquad (2)$$

It is believed that at the test temperature of 800°C, only $AgCrO_2$ was formed in the porous layer; however, due to the slow furnace cooling rate (~1.25°C/min) seen by the test cells, the reverse reaction of Eq. 2 occurred, resulting in the large amounts of $Ag_2CrO_4$ observed by SEM at room temperature. It is not clear if the Mn dopant released from the interconnect alloy has any effect on the stability of $Ag_2CrO_4$ or $AgCrO_2$; however, a higher amount of Mn was detected in $AgCrO_2$ [i.e. forming $Ag(Cr,Mn)O_2$] than in $Ag_2CrO_4$. It should be noted that the amount of Ag observed in the contact layer and porous cathode after 500-h exposure at 800°C was so significant, that it could not explained by the Ag evaporation from Ag in the composite alone. It is possible that the interaction between Ag and Cr near the interface between the interconnect and contact layer first caused the formation of $AgCrO_2$, which might have a much higher evaporation rate than that of pure Ag, leading the accelerated Ag contamination in the contact layer as well as the porous cathode. Additional work is clearly needed to assess the phase stability and the evaporation behavior of $AgCrO_2$.

Based on the experimental results, the high Ag-content contact materials are poor choices for use with stainless steel interconnects due to extensive contamination of the Ag-Cr-O phases in the LSM cathode layer of these test cells. Even though these materials exhibit the lowest, most stable ASRs of all the contact materials tested, extensive penetration of $Ag(Cr,Mn)O_2$ into the porous LSM cathode layer will assuredly harm cell performance by blocking oxygen diffusion pathways in the cathode, thus reducing the active area in the cathode. This would cause the fuel cell to maintain relatively high conductivity and yet have poor power density. Increasing the content of the perovskite in the composite contact might inhibit Cr migration and thus reduce the formation of $AgCrO_2$.

### *2.2.5 Comparison of Cr Migration for Different Composite Contact Materials*

Cr migration was evaluated by quantifying the atomic percentage of Cr in each contact layer and its adjacent cathode layer using SEM/EDS. Figure 23 shows a comparison of the amount of chromium present in cathode and contact layers for cells with different contact materials subjected to thermal cycling and isothermal exposure. The general trend observed in the data was that a higher percentage of perovskite in the composite contact layer resulted in a lower amount of Cr detected in the contact material and the adjacent cathode layer. Furthermore, higher amounts of Cr are present in the contact layer than in the adjacent cathode layer. However, there are a few more subtle trends that will be discussed further.

For the Ag-LSM composites under cyclical exposure conditions, the amount of Cr present in the contact material was just slightly higher than the amount detected in the adjacent cathode material. This seems to indicate that LSM is not very effective at trapping Cr within the contact material and preventing further spread to the cathode. However, it has been widely observed that volatilized chromium vapor species readily react with LSM to form both $(Mn,Cr)_3O_4$ and $(La,Sr)(Cr,Mn)O_3$ in SOFC environments [28-30]. The work by Jiang et al. [31] demonstrated that Cr deposition at the LSM/YSZ interface was primarily due to the generation of $Mn^{2+}$ ions during cathodic polarization, which readily reacted with the $CrO_3$ vapor species to form $(Mn,Cr)_3O_4$ on the YSZ surface. This not only confirmed the reactivity of LSM with Cr vapor species but also indicated that the Mn-Cr spinel was not captured by or attached to the LSM surface; rather, the spinel deposited preferentially on the yttria-stabilized zirconia (YSZ).

Furthermore, it is quite apparent that the formation and deposition of $Ag_2CrO_4$ is also a significant source of the chromium contamination observed in the LSM cathode materials, especially for the contact materials with high Ag content. On the other hand, for the Ag-LSM composites after isothermal testing, there was a noticeably greater amount of chromium present in the contact material than in the LSM cathode. This could be attributed to the reduced amount of thermal stresses and cracking within the contact layer under isothermal conditions, resulting in a less effective pathway for Cr migration into the cathode material.

For the Ag-LSCF composites, there is a clear disparity in the amount of chromium present in the contact material compared to that in the adjacent LSM cathode material for

both isothermally and cyclically tested cells. A substantially higher amount of Cr was detected in the contact material than in the cathode, indicating that LSCF reacts with the migrating Cr species and effectively traps them within the contact layer. The formation of $SrCrO_4$ crystals was widely reported in Co-containing perovskites such as $(La,Sr)CoO_3$ (LSC) and LSCF following exposure to Cr-containing vapors at elevated temperatures [32-34], and it is believed that this reaction is the primary mechanism for Cr capture in the Ag-LSCF composite contact materials. The mechanism for Cr reactivity in LSCF differs from that of LSM in that the $SrCrO_4$ crystals form directly on the surface of LSCF, effectively capturing the Cr and preventing further Cr migration within the cell [35]. It is also possible that some Cr could have become incorporated into the perovskite structure of the contact material in the form of $(La,Sr)(Co,Cr,Fe)O_3$, since Cr is commonly utilized as a B-site dopant in many perovskites [36, 37].

The ability of LSCF to absorb Cr and inhibit it from poisoning the cathode makes it a more desirable candidate for use in contact materials than LSM. In commercial applications where the use of Cr-containing ferritic interconnect alloys is desired to reduce initial costs, LSCF-containing composite contact layers in conjunction with Cr-retaining interconnect coatings and Cr-tolerant cathode materials could be a feasible solution to achieving stable long-term performance. For stationary power applications with long periods of isothermal holding, LSCF contact materials with 0-25 vol.% Ag addition can yield suitable ASR performance while greatly inhibiting Cr migration, while for portable power applications with frequent thermal cycling, LSCF contact materials with at least 25 vol.% Ag addition are probably necessary to maintain acceptably low ASR levels within the stack operation lifetime.

### 2.3 Conclusions

The following conclusions can be drawn based on this study:

1. The effects of exposure time/temperature, gas flow rate, and environment on the evaporation of pure Ag at 750-900°C were studied. The Ag evaporation rate increased linearly with air flow rate initially and became constant for the air flow rate $\geq \sim 1.0$ cm·s$^{-1}$.
2. An activation energy of 280 KJ.mol$^{-1}$ was obtained for Ag evaporation in both air and Ar+5%$H_2$+3%$H_2O$. The exposure environment had no measurable influence on the Ag evaporation rate as well as its dependence on the gas flow rate, while different surface morphological features were developed after thermal exposure in the oxidizing and reducing environments.
3. Pure Ag is not suitable for long-term SOFC contact application due to its excessive evaporation rate. Furthermore, pure Ag contact materials interacted negatively with Cr-containing steel interconnects, readily forming $Ag_2CrO_4$ and $AgCrO_2$, which clog the porous cathode and reduce the amount of active sites available for oxygen reduction.
4. Alloying additions with various transition metals to Ag as well as insertion of a perovskite phase into Ag to form a composite material did not significantly affect the Ag evaporation rate. Noble metal additions to Ag were effective in reducing

Ag evaporation rate. However, they are too costly to justify their application in commercial SOFC stacks.

5. The Ag-LSM composite contact materials exhibited higher overall ASR's than those of Ag-LSCF. The addition of as little as 10 vol.% Ag into perovskite contact materials resulted in an order of magnitude reduction in ASR degradation rates.
6. Isothermally-tested cells exhibited much more stable ASR's than thermally-cycled cells, which degraded rapidly due to the accumulation of damage caused by thermal stress generation during heat-up and cool-down.
7. LSCF was a more effective "chromium-getter" than LSM due to its ability to absorb Cr in the contact layer, resulting in much lower levels of Cr in the cathode layer.
8. Composite contact materials with high amounts of LSM proved to cause severe oxidation of the ferritic Crofer 22 APU interconnect (especially when subjected to thermal cycling conditions), resulting in rapid ASR degradation.
9. The Ag-LSCF composites are an overall better choice as contact materials than the Ag-LSM materials, as they maintained acceptably low ASR's and inhibited Cr-migration into the adjacent cathode layer.

## 3. GRAPHIC MATERIALS LIST

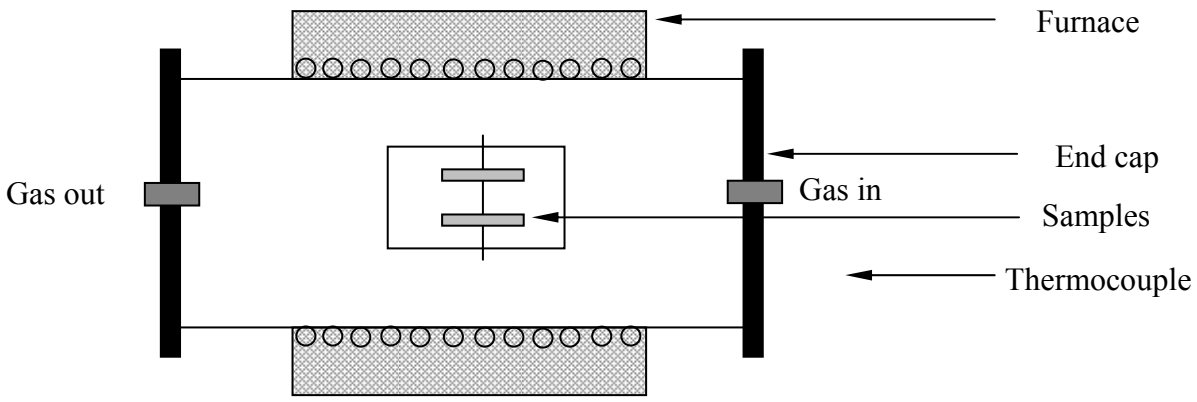


**Fig. 1 Schematic of the evaporation test rig**

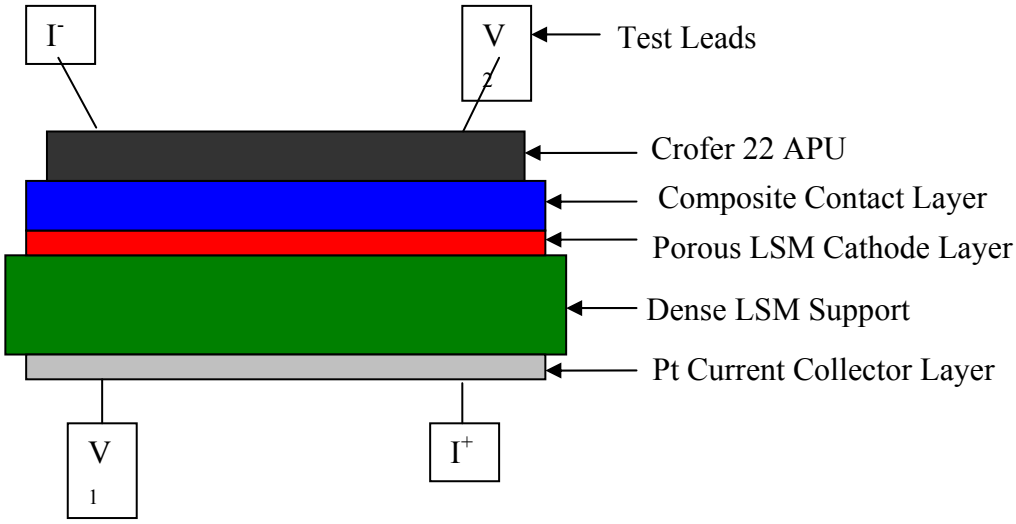


**Fig. 2 Schematic of a test cell for evaluating various composite contact materials**

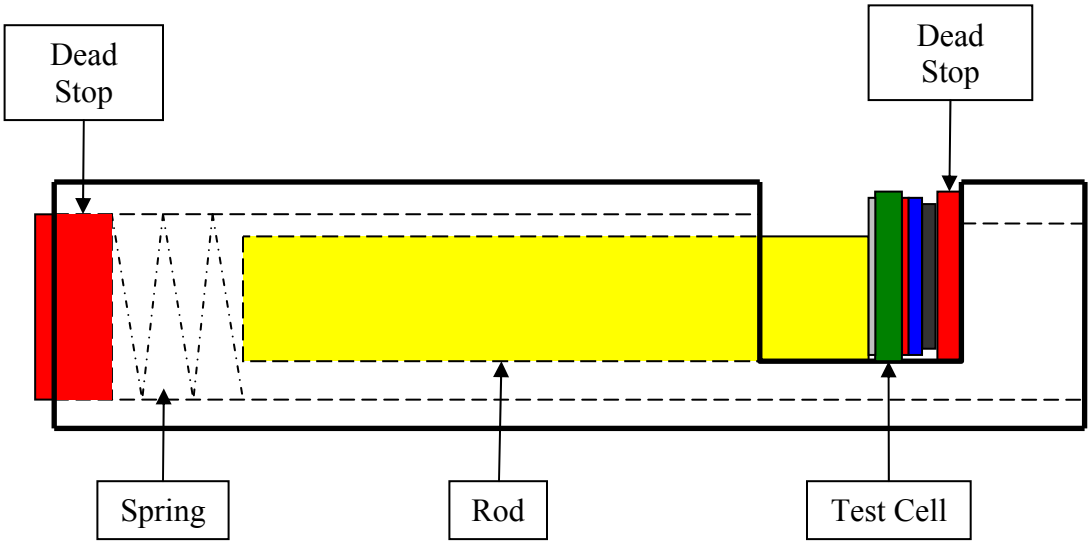


**Fig. 3 Schematic of a sample holder**

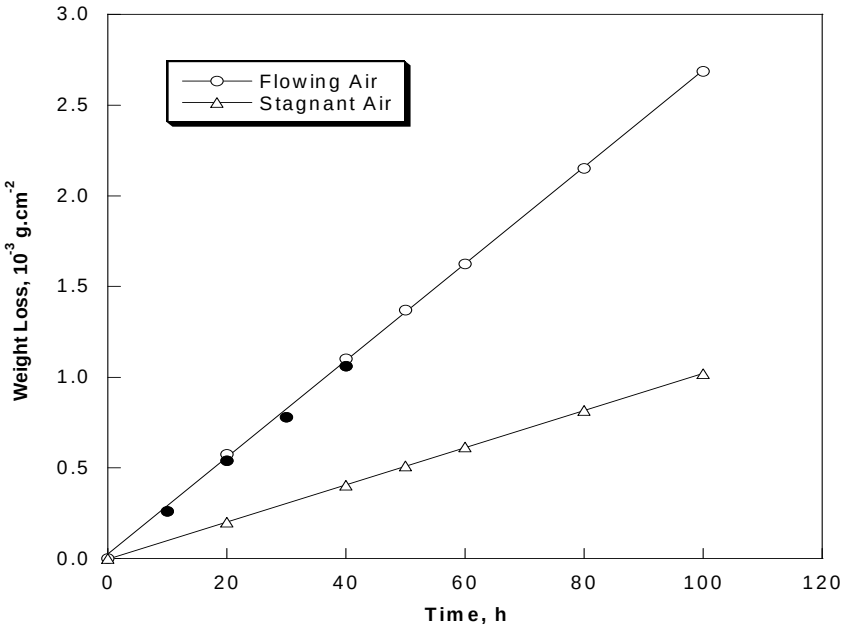


**Fig. 4 Weight losses of the Ag samples in both stagnant air and flowing air with a flow rate of 1.56 cm·s$^{-1}$ after various durations of exposure at 900°C. Data points (shown with solid symbol) were obtained in Ar+5%$H_2$+3%$H_2O$ at 900°C.**

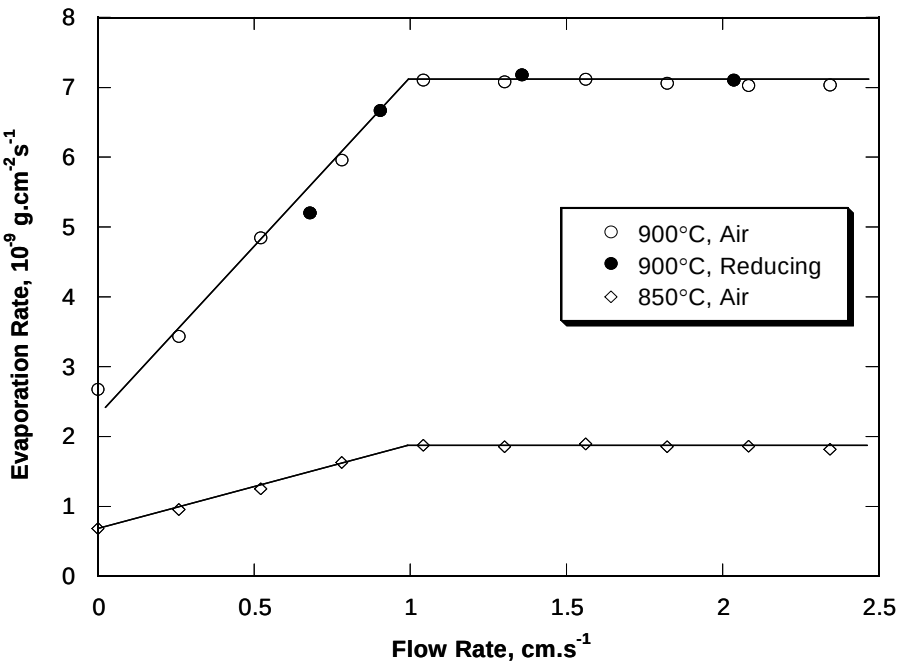


**Fig. 5 Evaporation rate of Ag as a function of air flow rate at 900°C and 850°C. Data points (shown with solid symbol) obtained in Ar+5%$H_2$+3%$H_2O$ at 900°C.**

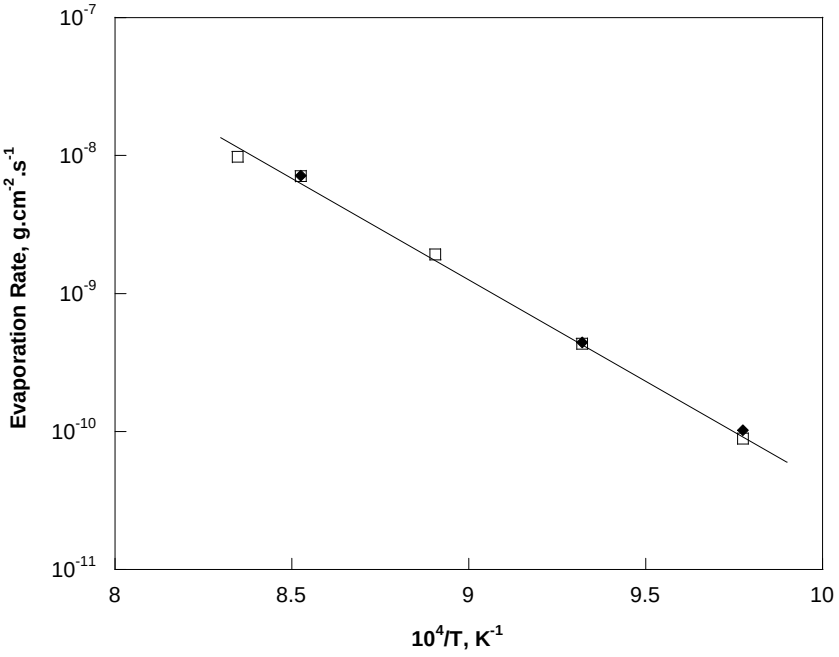


**Fig. 6 Evaporation rate of Ag as a function of temperature in air with a flow rate of 1.56 cm·s$^{-1}$. Data points (shown with solid symbol) obtained in Ar+5%$H_2$+3%$H_2O$.**

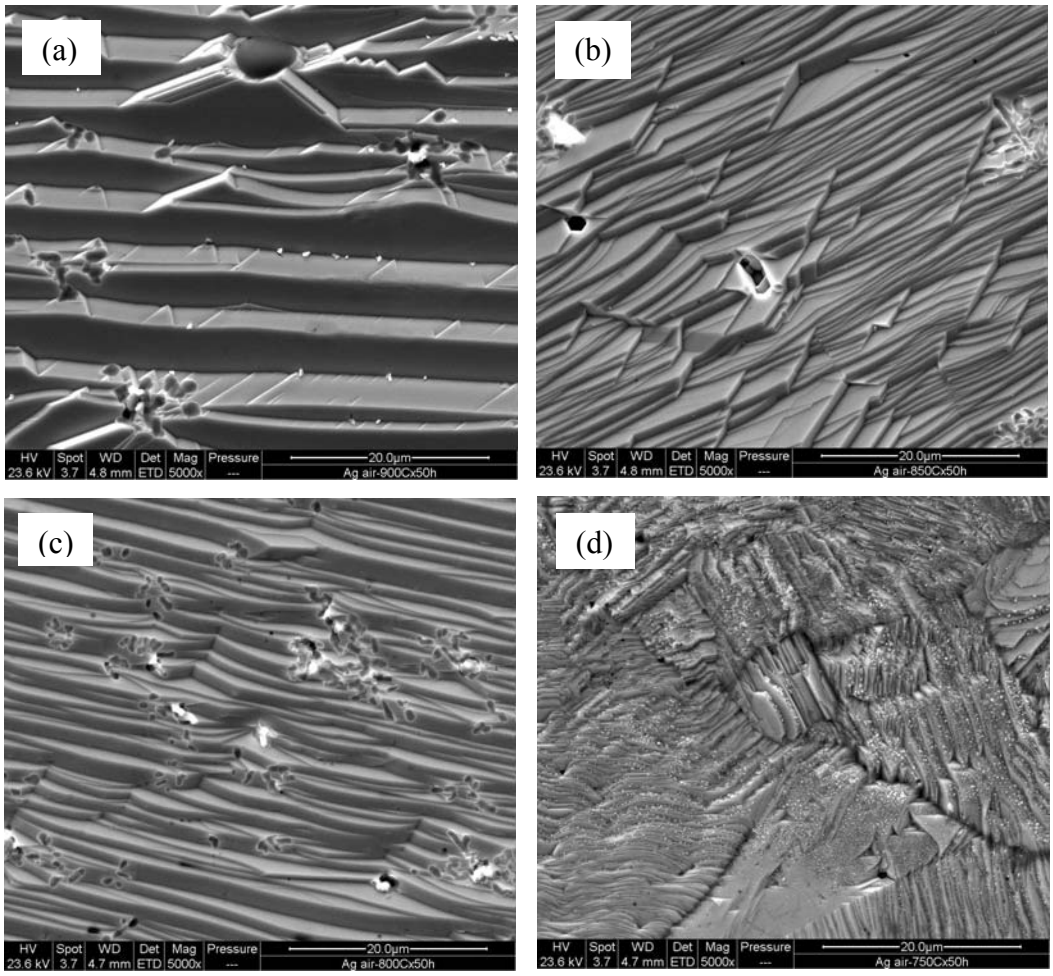


**Fig. 7 Surface striations of Ag developed after thermal exposure for 50 h in air with a flow rate of 1.56 cm·s$^{-1}$: (a) 900°C; (b) 850°C; (c) 800°C; and (d) 750°C**

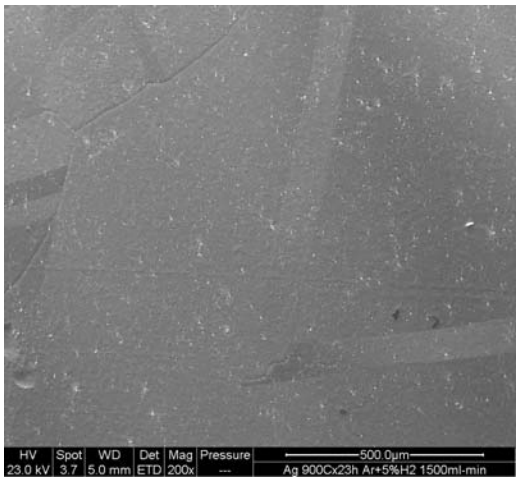


**Fig. 8 Smooth surface of Ag developed after thermal exposure at 900°C for 20 hours in Ar+5%$H_2$ with a flow rate of 1.56 cm·$s^{-1}$**

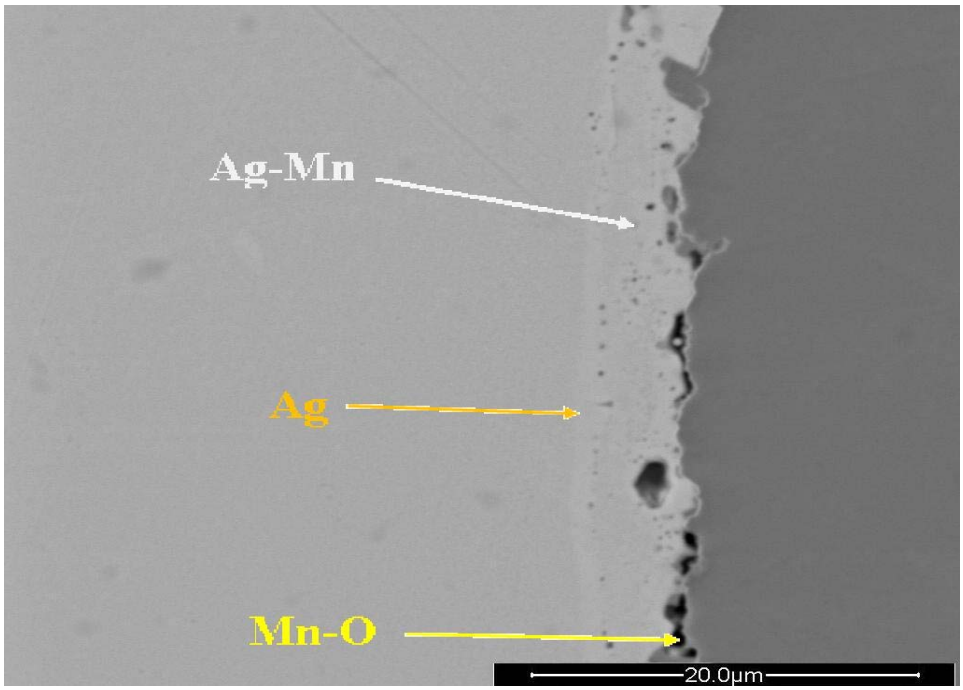


**Fig. 9 Cross-sectional view of the Ag- 5% Mn alloy after exposure for 200 hours**

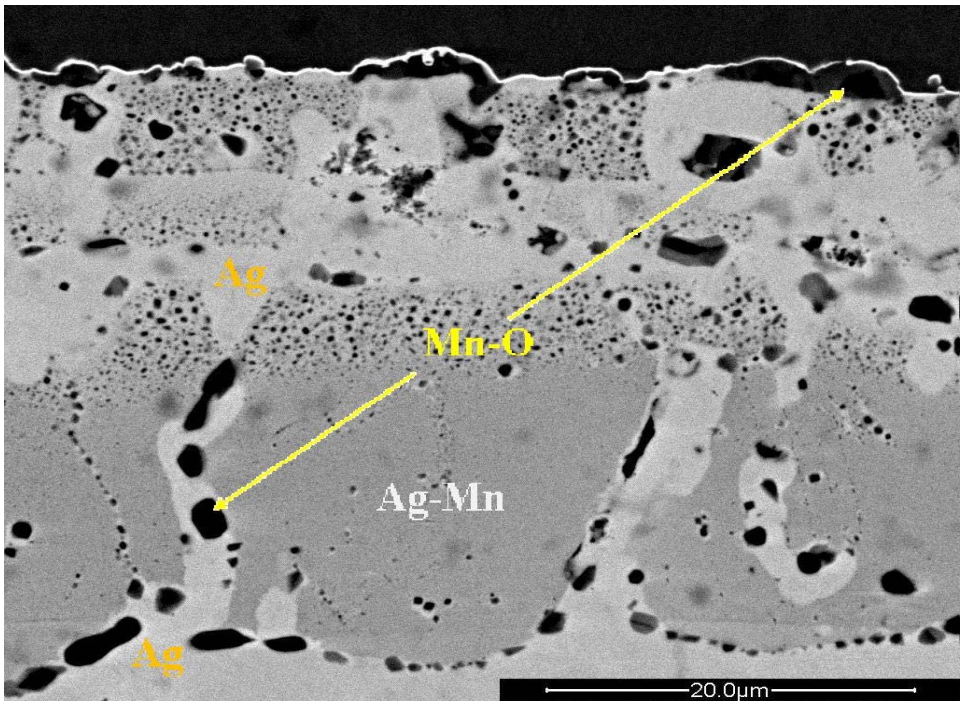


**Fig. 10 Cross-sectional view of the Ag- 15% Mn alloy after exposure for 150 hours**

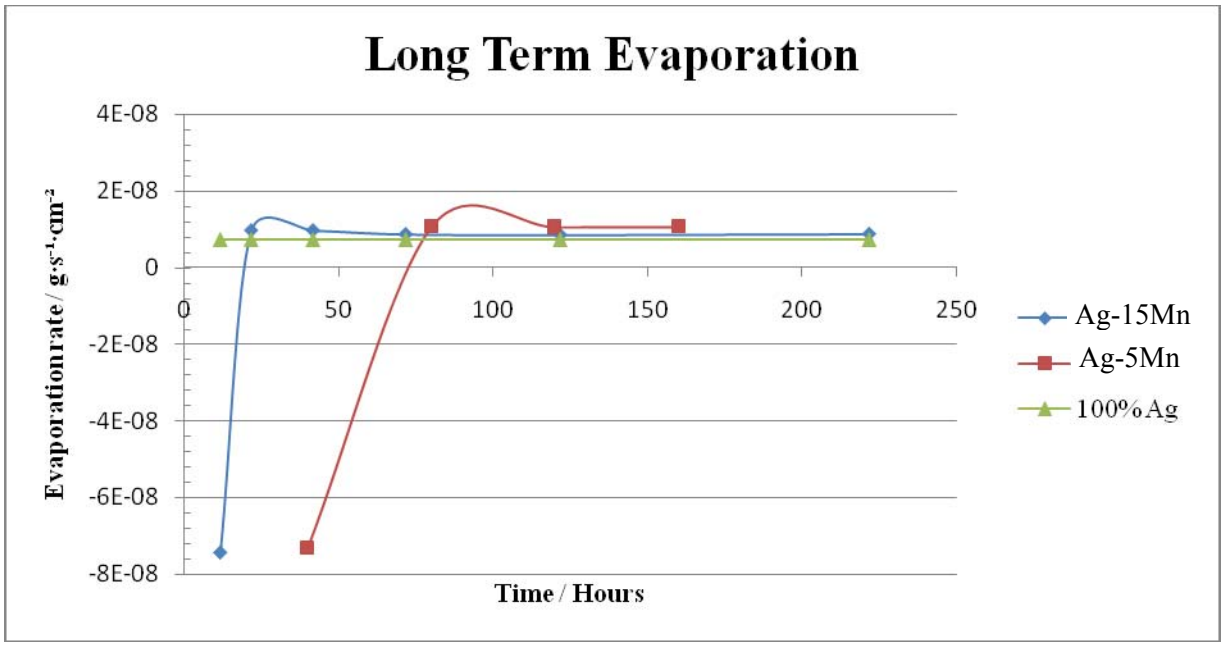


**Fig. 11 Evaporation rate of Ag-Mn samples as a function of exposure time**

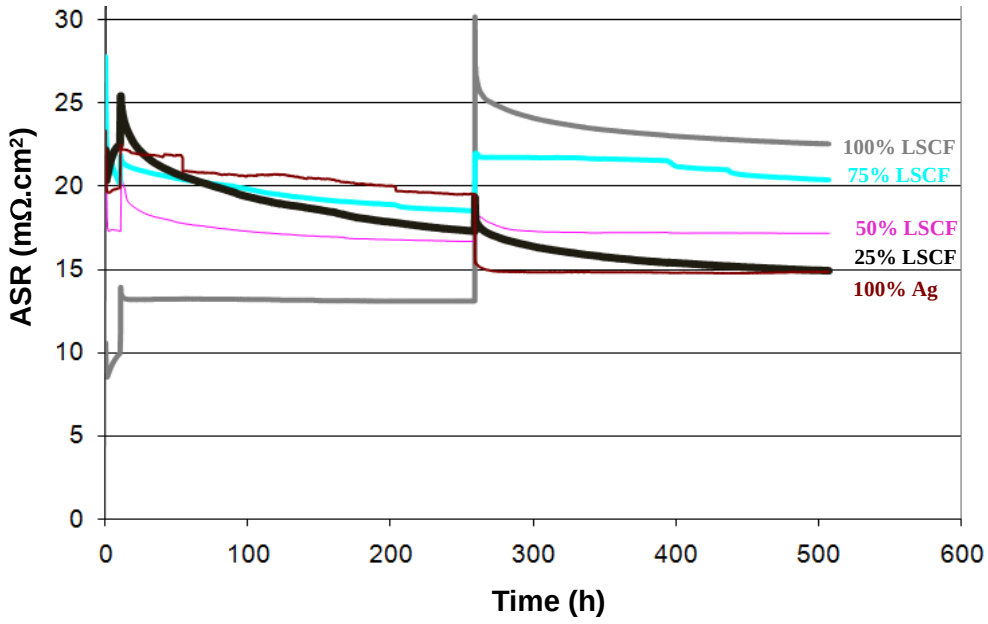


**Fig. 12 ASR response of the cells with the Ag-LSCF composite contact materials during isothermal exposure at 800°C in air for about 500 hours. The data collected during the initial sintering at 850°C for 10 h were also included in the plot. A single cool-down event after 250 hours was added in the testing.**

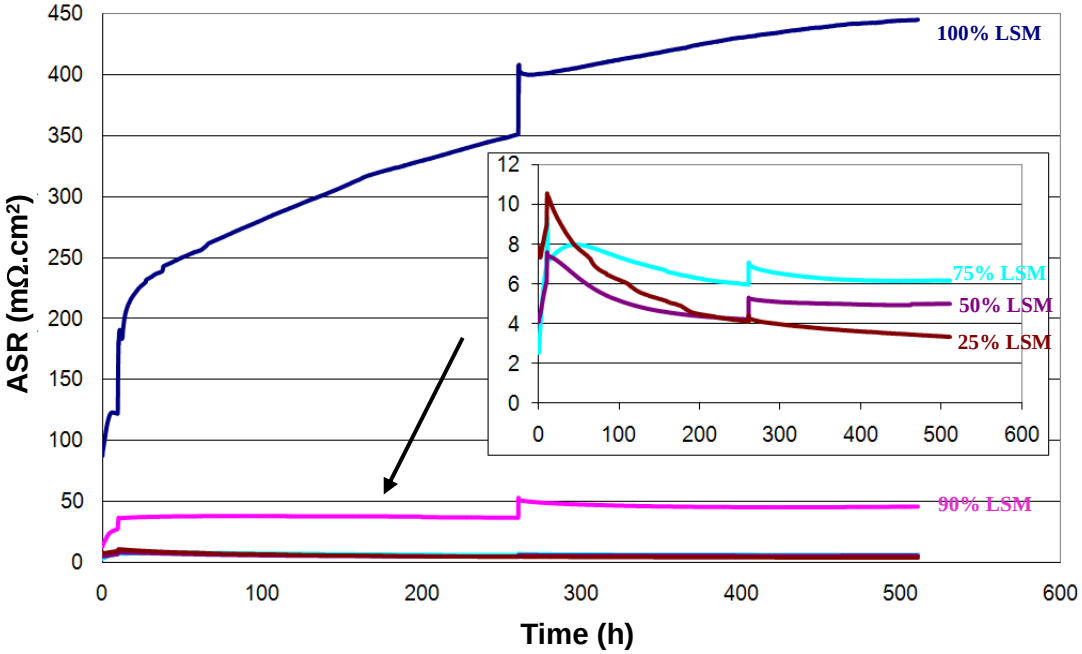


**Fig. 13 ASR response of the cells with the Ag-LSM composite contact materials during isothermal exposure at 800°C in air for about 500 hours. The data collected during the initial sintering at 850°C for 10 h were also included in the plot. A single cool-down event after 250 hours was added in the testing.**

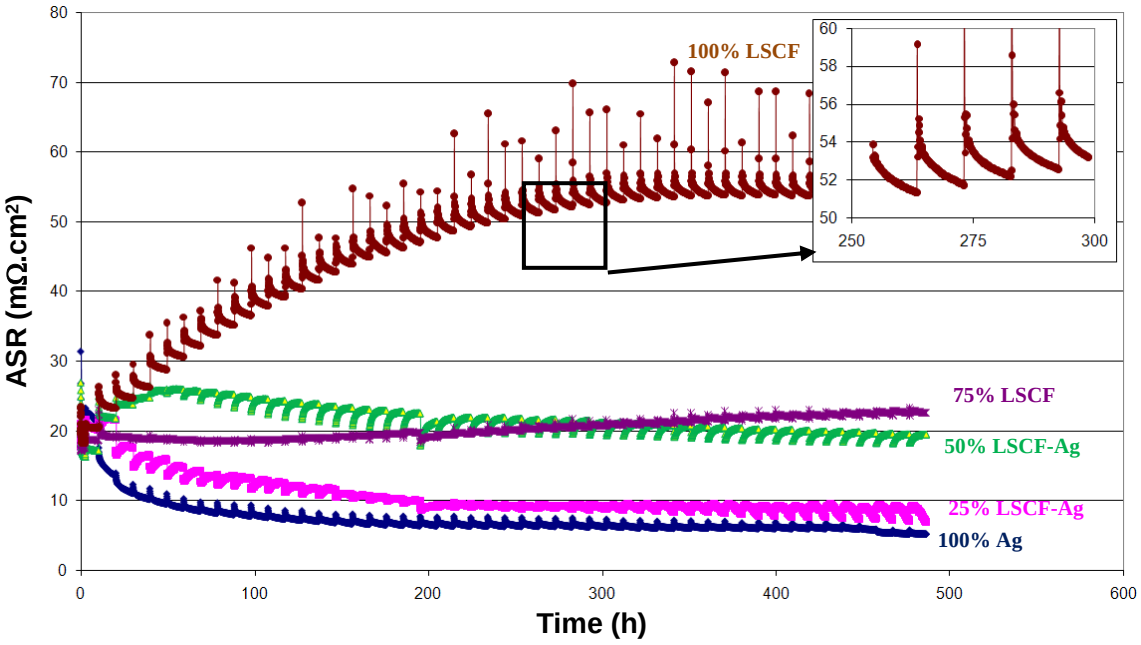


(a)

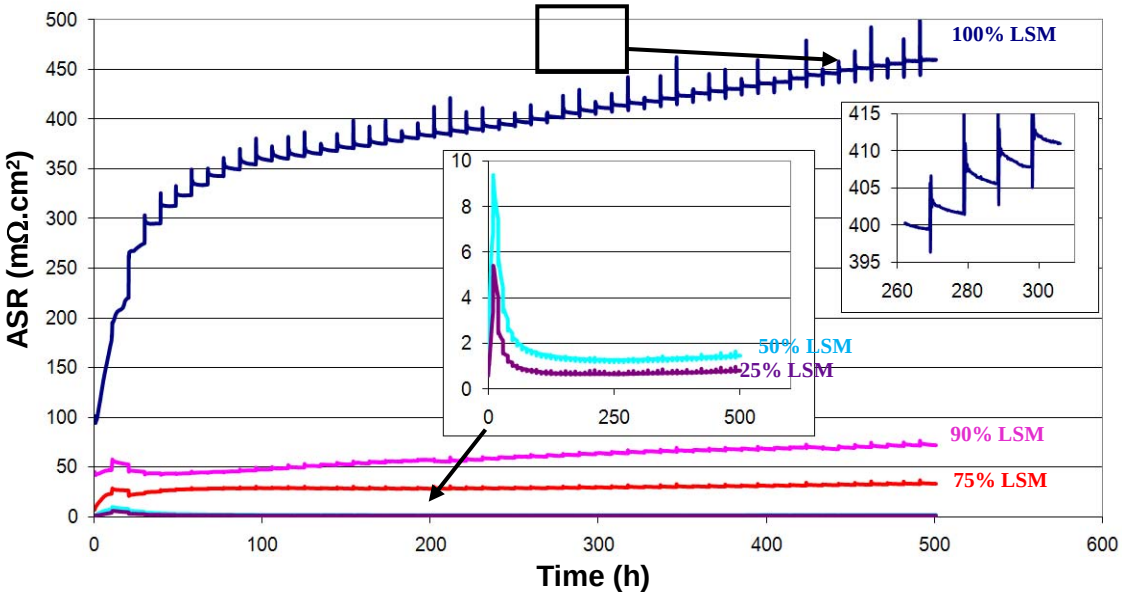


(b)

**Fig. 14 ASR response of the cells with (a) the Ag-LSCF composite and (b) the Ag-LSM composite contact materials at 800°C during thermal cycling. Each cycle consisted of holding at 800°C for 10 h before furnace cooling to 250°C and subsequent heat-up to 800°C. A total of 50 thermal cycles with 500 cumulative hours of exposure at 800°C were completed for each cell.**

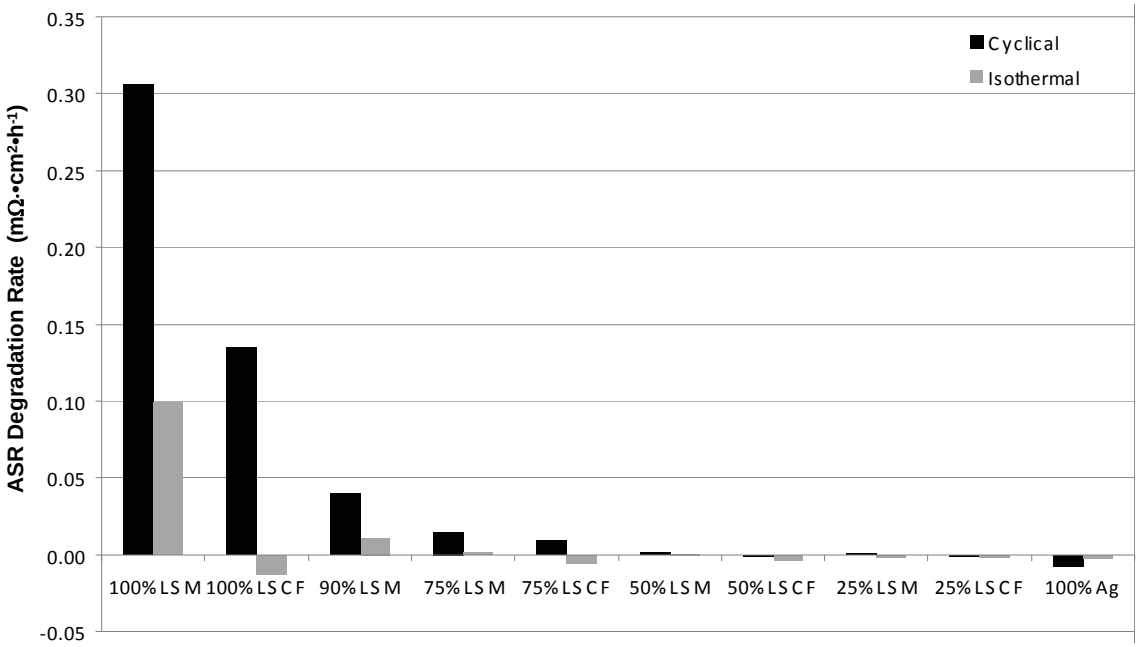


**Fig. 15 Comparison of ASR degradation rates of the various cells under the isothermal and cyclical testing conditions as determined from the slope of the ASR curve during the final 100 hours at 800°C.**

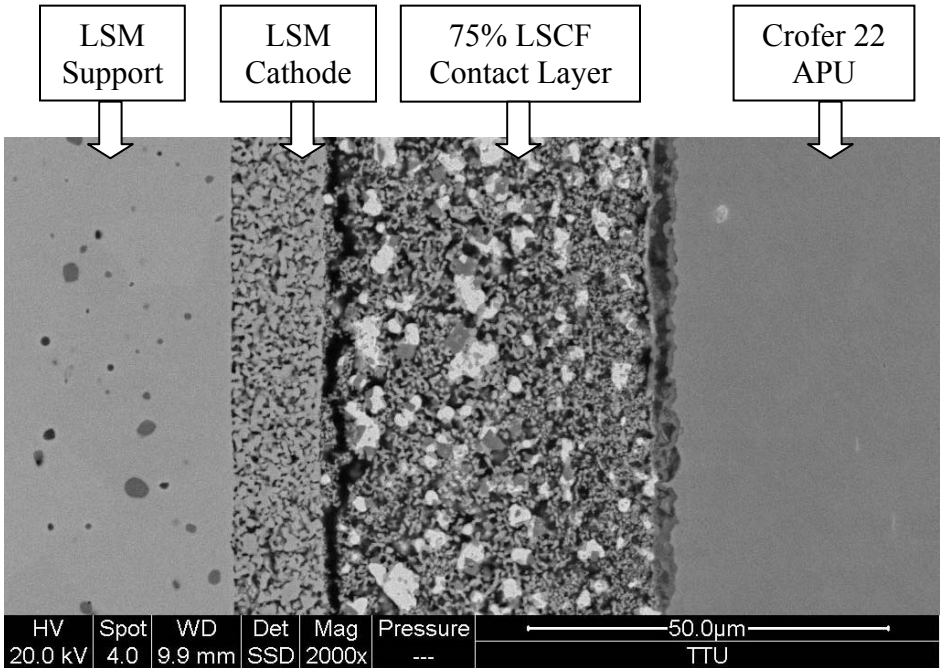


**Fig. 16 Cross section of a test cell with 75 vol.% LSCF contact layer after isothermal exposure for 500 h at 800°C.**

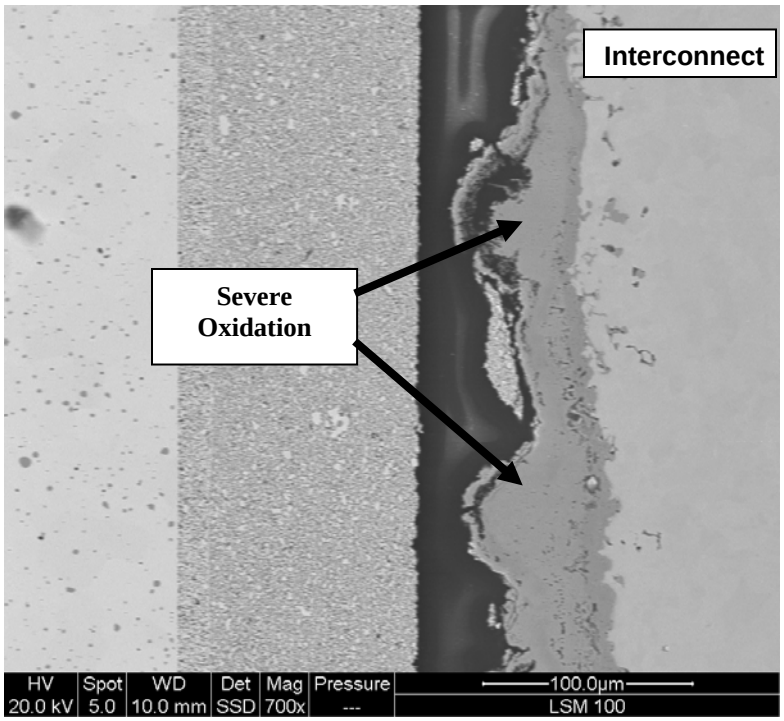


**Fig. 17 Abnormal growth of the oxide scale on the Crofer 22 APU alloy during thermal cycling for 500 h at 800°C.**

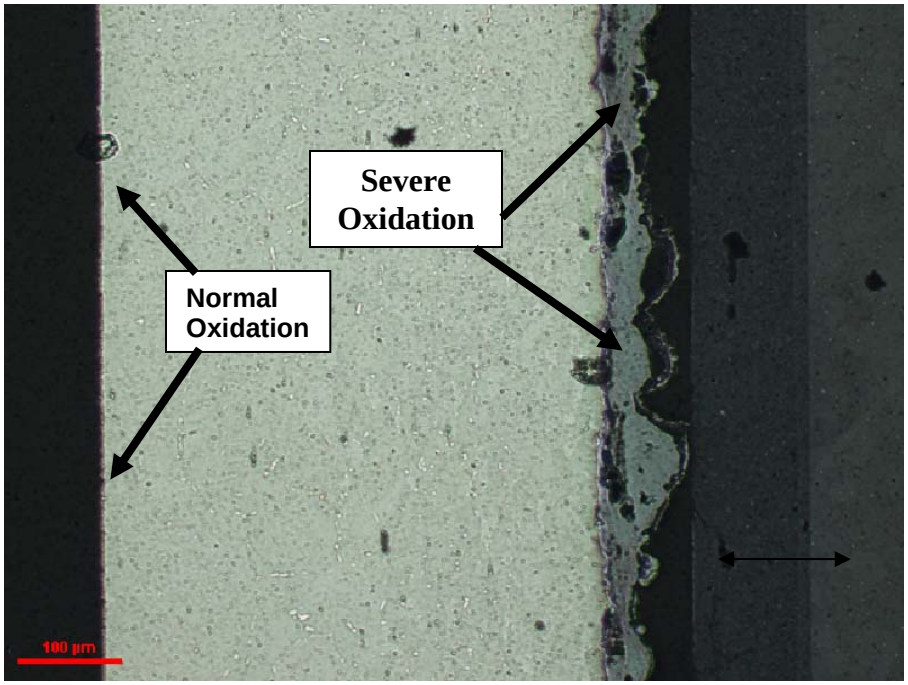


**Fig. 18 Oxide scale on top of the interconnect with 100% LSM contact layer after thermal cycling for 500 h at 800°C**

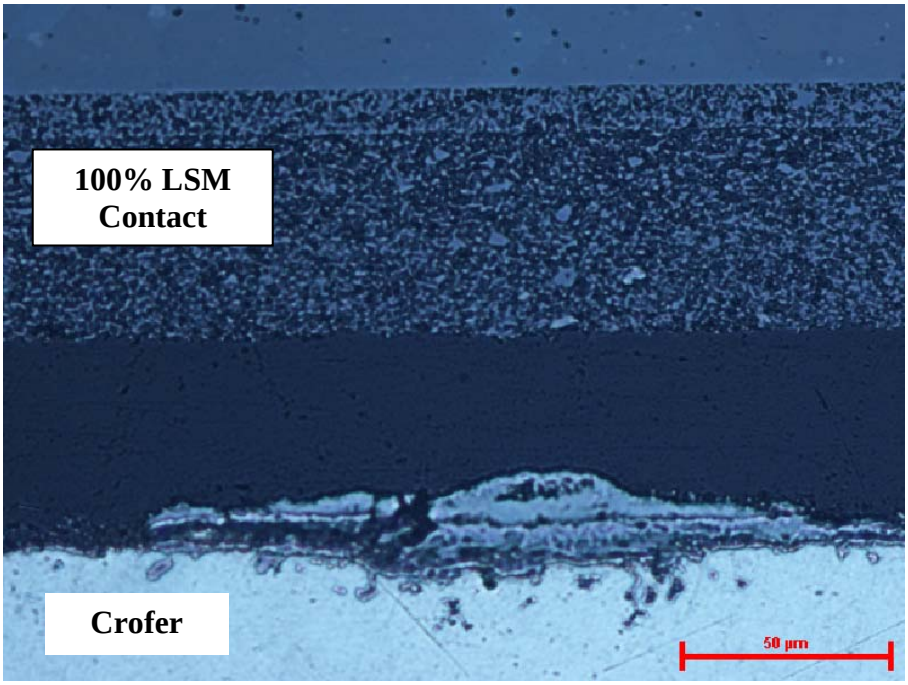


**Fig. 19 The oxide scale formed on Crofer 22 APU interconnect alloy in contact with the 100% LSM contact layer during isothermal exposure at 800°C.**

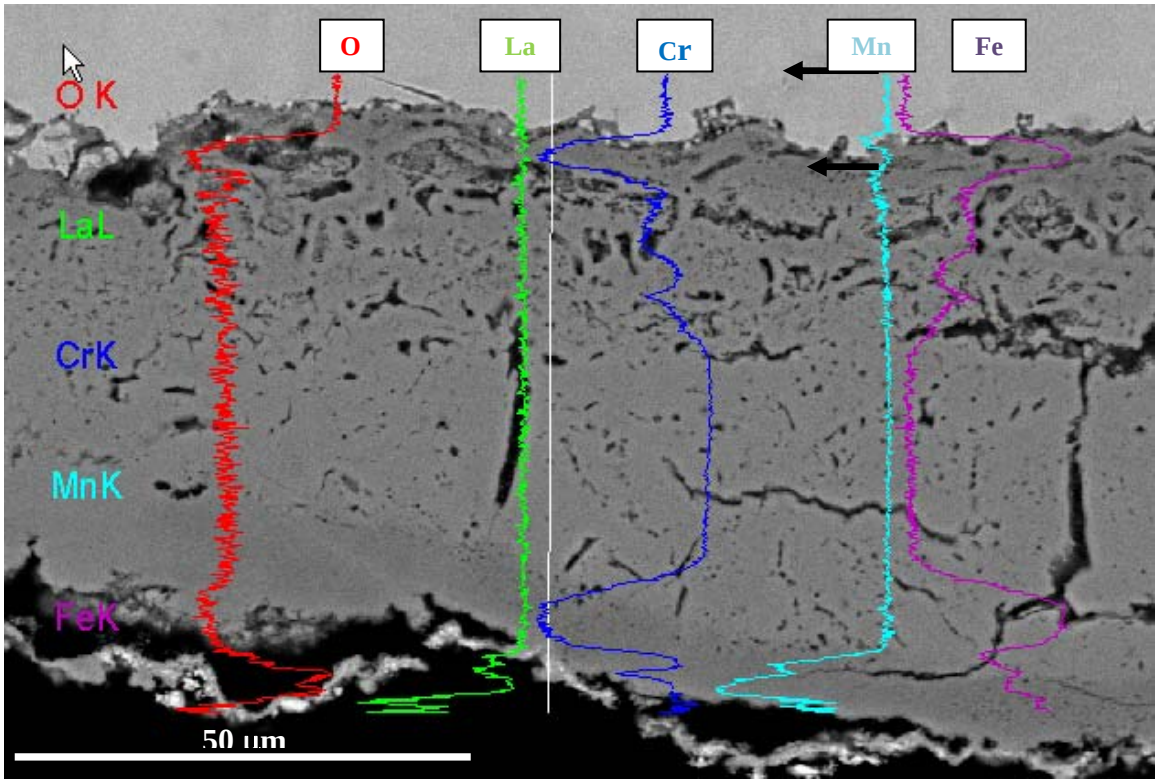


**Fig. 20 Line scan of the abnormal oxide scale formed on Crofer 22 APU during thermal cycling for 500 h at 800°C.**

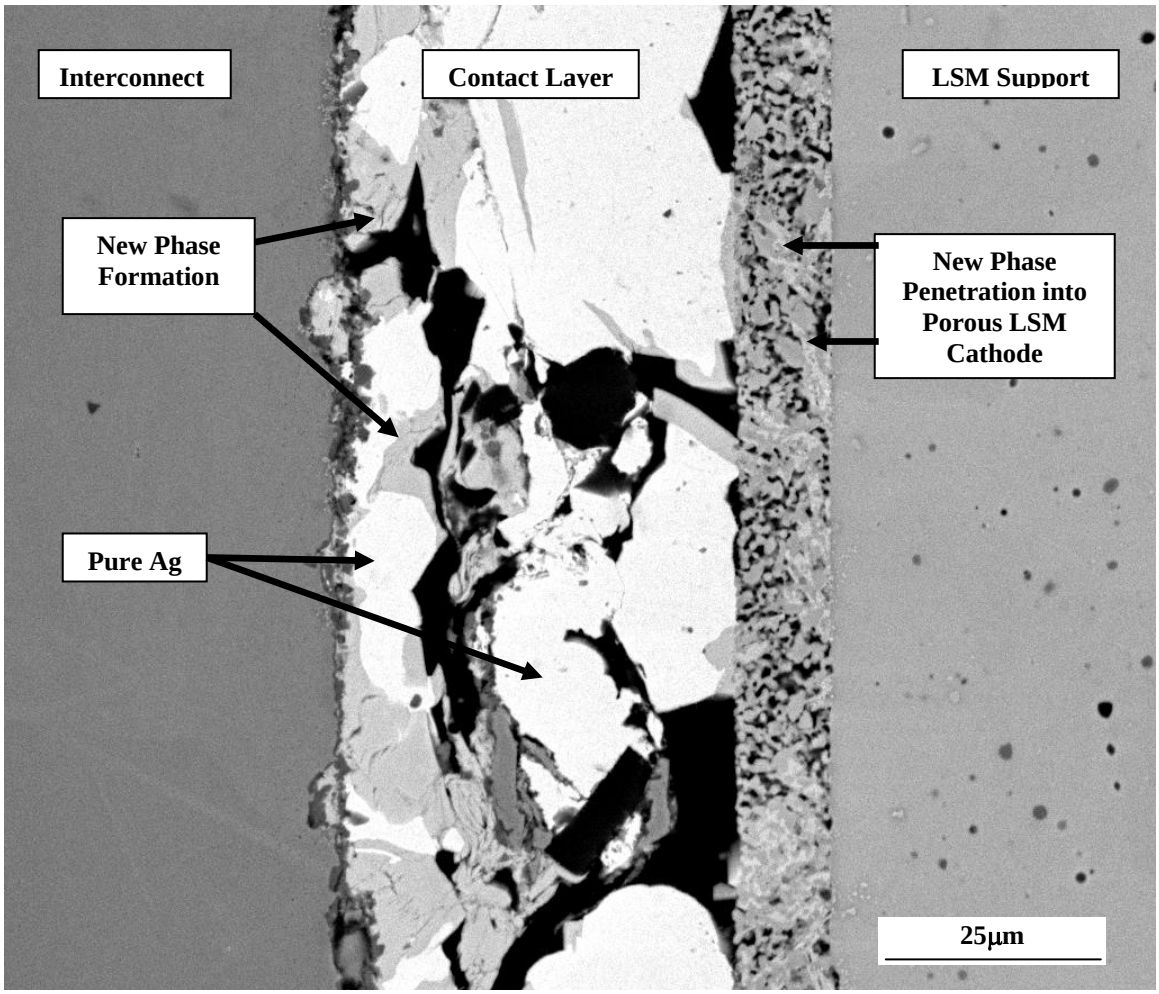


**Fig. 21 Cross-sectional view of the cell with the 100% Ag contact layer after thermal cycling for 500 h at 800°C.**

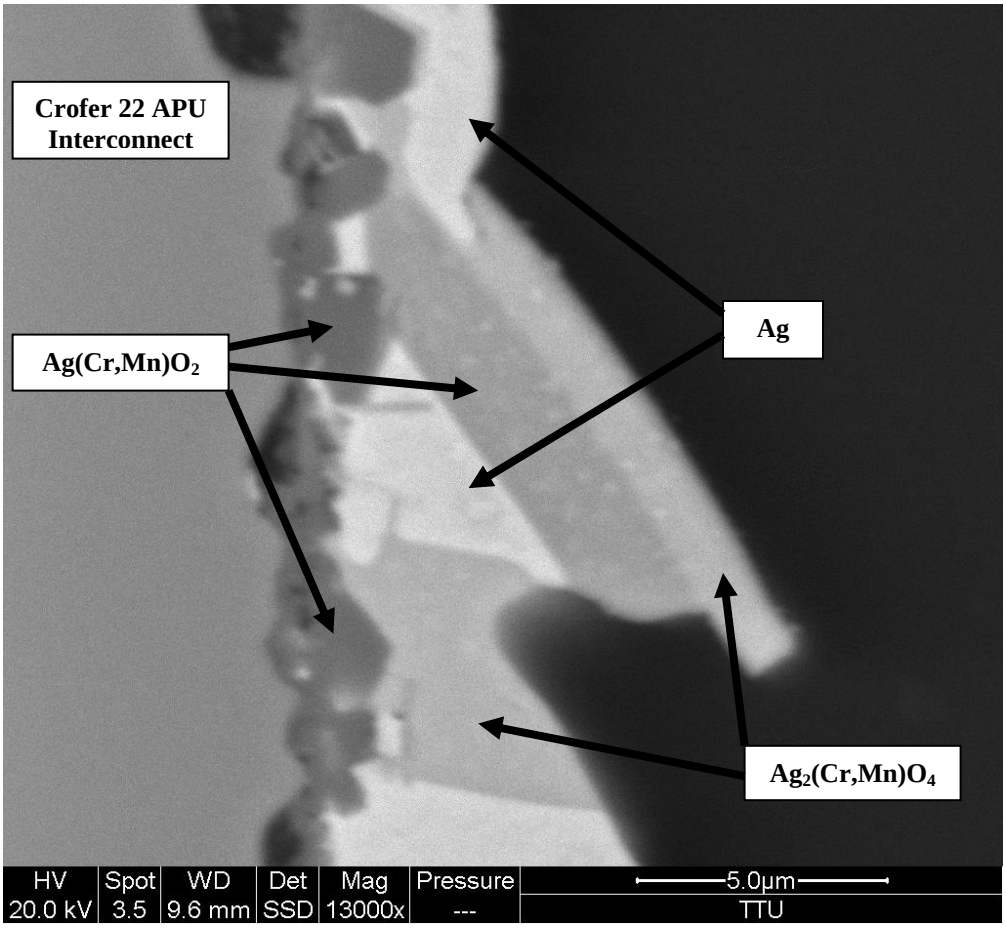


**Fig. 22 Cross-sectional view showing the presence of multiple phases in the 100% Ag contact material after thermal cycling for 500 h at 800°C.**

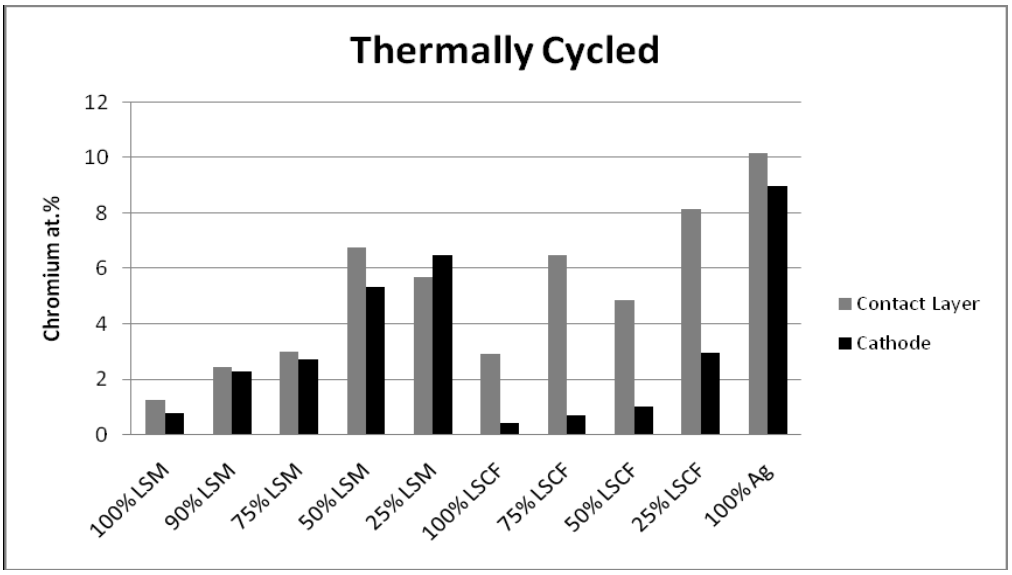


(a)

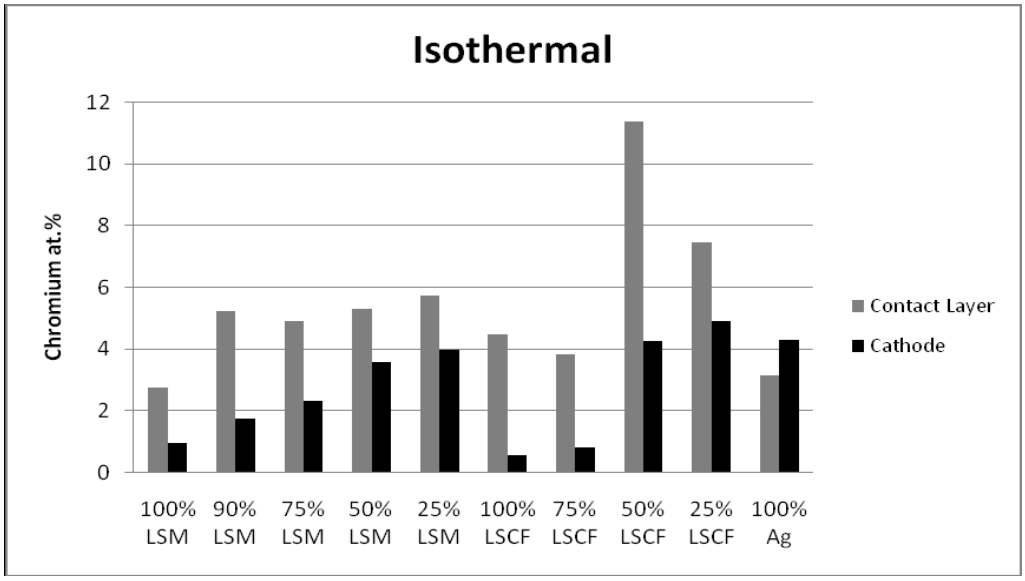


(b)

**Fig. 23 Chromium content in the contact and cathode layers of the cells with different contact materials thermally-exposed to air for 500 h at 800°C: (a) under thermal cycling condition; and (b) under isothermal exposure condition.**

## 4. REFERENCES


1. W. L. Winterbottom and J. P. Hirth, in *Condensation and Evaporation of Solids*, E. Rutner, P. Goldfinger, and J. P. Hirth, Editors, p. 347, Gordon and Breach Science Publishers, Inc., New York (1964).
2. E. D. Hondros and A. J. W. Moore, Acta Metall., 8, 647 (1960)
3. C. Gindorf, L. Singheiser, and K. Hilpert, J. Phys. Chem. Solids, 66, 384 (2005).
4. C. L. McCabe and C. E. Birchenall, Trans. AIME, 197, 707 (1953)
5. W. L. Winterbottom, J. Appl. Phys., 40, 3803 (1969)
6. J. A. A. Leroux and E. Raub, Z. Anorg. Allgem. Chem., 188, 205 (1930)
7. W. A. Meulenberg, O. Teller, U. Flesch, H. P. Buchkremer, and D. Stöver, J. Mater. Sci., 36, 3189 (2001)
8. B. Chalmers, R. King, and R. Shuttleworth, Proc. Roy. Soc. A, 193, 465 (1948)
9. G. Wulff, Z. Kristallogr., 34, 449 (1901)
10. A. J. W. Moore, Acta Metall., 6, 293 (1958)
11. E. Konysheva, J. Laatsch, E. Wessel, F. Tietz, N. Christiansen, L. Singheiser, and K. Hilpert. Solid State Ionics, V 177, 9-10, 923 (2006)
12. F. Tietz, A. Mai, and D. Stover, Solid State Ionics, 179, 1509 (2008)
13. K. Murata, T. Fukui, H. Abe, M. Naito, and K. Nogi, J. Power Sources, 145, 257 (2005)
14. Z. Lei, Q. Zhu, and L. Zhao, J. Power Sources, 161, 1169 (2006)
15. F. Tietz, and D. Sebold, Mater. Sci. Eng. B, 150, 135 (2008)
16. S. Kuharuangrong, T. Dechakupt, and P. Aungkavattana, Mater. Lett., 58, 1964 (2004)
17. R. N. Basu, S. K. Pratihar, M. Saha, and H. S. Maiti, Mater. Lett., 32, 217 (1997)
18. P. Piccardo, P. Gannon, S. Chevalier, M. Viviani, A. Barbucci, G. Caboche, R. Amendola, and S. Fontana, Surf. Coat. Technol., 202, 1221 (2007)
19. S. Fontana, R. Amendola, S. Chevalier, P. Piccardo, G. Caboche, M. Viviani, R. Molins, and M. Sennour, J. Power Sources, 171, 652 (2007)
20. Z. Yang, G. Xia, P. Singh, and J. W. Stevenson, J. Power Sources, 155, 246 (2006)
21. P. Ho and H. Huntingtion. J. Phys. Chem. Solids, 27, 1319 (1966)
22. S. P. Simner, M. D. Anderson, J. W. Templeton, and J. W. Stevenson, J. Power Sources, 168, 236 (2007)
23. S.P. Simner, M.D. Anderson, L.R. Pederson, and J.W. Stevenson, J. Electrochem. Soc., 152, A1851-1859 (2005)
24. Y. Niu, J. X. Song, F. Gesmundo, and G. Farne, Oxid. Met., 55, 3/4 (2001).
25. M. Cieslak-Golonka, J. Therm. Anal., 38, 2501 (1992)
26. H. W. Abernathy, E. Koep, C. Compson, Z. Cheng, and M. Liu, J. Phys. Chem. C, 112, 13299 (2008)
27. C. Tedmon, H. Spacil, and S. Mitoff, J. Electrochem. Soc., 116, 1170 (1969)

28. S. P. Badwal, R. Deller, K. Foger, Y. Ramprakash, and J. P. Zhang, Solid State Ionics, 99, 297 (1997)
29. T. Komatsu, R. Chiiba, H. Arai, and K. Sato, J. Power Sources, 176, 132 (2008)
30. E. Konysheva, H. Pankalla, E. Wessel, J. Mertens, U. Seeling, L. Singheiser, and K. Hilpert. J. Electrochem. Soc., 153, A765 (2006)
31. S.P. Jiang, S. Zhang, and Y.D. Zhen, J. Mater. Res., 20, 747 (2005)
32. S. P. Jiang and Y. Zhen, Solid State Ionics, 179, 1459 (2008)
33. S.P. Jiang, J.G. Love, and L. Apateanu, Solid State Ionics, 160, 15 (2003)
34. H. Yokokawa, N. Sakai, T. Horita, K. Yamaji, M. E. Brito, and H. Kishimoto. J. Alloys Compd., 452, 41 (2008)
35. S.P. Jiang, S. Zhang, and Y.D. Zhen, J. Electrochem. Soc., 153, 127 (2006)
36. T. Nagai, W. Ito, and T. Sakon. Solid State Ionics, 177, 3433 (2007)
37. T. Yao, Y. Uckimoto, T. Sugiyama, Y. Nagai. Solid State Ionics, 135, 359 (2000).

## 5. LIST OF ACRONYMS AND ABBREVIATIONS

SOFC - Solid oxide fuel cell
CTE - Coefficient of thermal expansion
ASR - Area specific resistance
EDS - Energy-dispersive spectroscopy
SEM – Scanning electron microscope
LSM - $(La_{0.8}Sr_{0.2})MnO_3$
$m\Omega \cdot cm^2$ - milliohm times square centimeter
LSCF: $(La_{0.6}Sr_{0.4})(Co_{0.8}Fe_{0.2})O_3$
YSZ-Yttria stabilized zirconia
$cm.s^{-1}$-Centimeters per second
$KJ.mol^{-1}$-Kilojoules per mole
°C-Degree Celsius
$g.cm^{-2}.s^{-1}$: Grams per centimeter squared per second
vol.% - volume percentage